Wavelet analysis of the self-similarity of diffusion-limited aggregates and electrodeposition clusters

F. Argoul, A. Arneodo, J. Elezgaray, and G. Grasseau
Centre de Recherche Paul Pascal, Avenue Schweitzer, Château Brivazac, 33600 Pessac, France

R. Murenzi
Institut de Physique Théorique, Université Catholique de Louvain, 1348 Louvain-la-Neuve, Belgium
(Received 11 September 1989)

We present the wavelet transform as a natural tool for characterizing the geometrical complexity of numerical and experimental two-dimensional fractal aggregates. We illustrate the efficiency of this "mathematical microscope" to reveal the construction rule of self-similar snowflake fractals and to capture the local scaling properties of multifractal aggregates through the determination of local pointwise dimensions $\alpha(\mathbf{x})$. We apply the wavelet transform to small-mass ($M \lesssim 5\times 10^4$ particles) Witten and Sander diffusion-limited aggregates that are found to be globally self-similar with a unique scaling exponent $\alpha(\mathbf{x})=1.60\pm 0.02$. We reproduce this analysis for experimental two-dimensional copper electrodeposition clusters; in the limit of small ionic concentration and small current, these clusters are globally self-similar with a unique scaling exponent $\alpha(\mathbf{x})=1.63\pm 0.03$. These results strongly suggest that in this limit the electrodeposition growth mechanism is governed by the two-dimensional diffusion-limited aggregation process.

I. INTRODUCTION

Pattern formation and growth process phenomena in systems far from equilibrium are the subject of increasing theoretical and experimental interest.[1-5] In recent years, much attention has been paid to characterize the geometrical properties of highly ramified clusters formed in apparently unrelated physical, chemical, and biological processes. In particular, a lot of effort has been devoted to establish the relationships between the cluster geometry and growth mechanisms. A number of models for cluster formation have been proposed to account for Laplacian fields that are common ingredients in a broad class of experimental situations[1-5] such as electrochemical deposition, fluid-fluid displacement in Hele-Shaw cells and porous media, formation of snowflakes and dendritic patterns, colloidal aggregation, fracture propagation, and dielectric breakdown. The prototype of these fractal growth models is the diffusion-limited aggregation (DLA) model introduced by Witten and Sander[6] in the early 1980s. In this model, particles are added, one at a time, to a growing cluster or aggregate of particles via random-walk trajectories. The structures generated by the DLA model exhibit branching over a wide range of length scales; the fractal dimension of these clusters was calculated both theoretically[7-10] and numerically,[6,11-17] and found to be less than the Euclidean dimension of the space in which the aggregation process takes place. Since the pioneering simulations of the DLA model, numerous extensions of the model were considered for various purposes,[17] e.g., to incorporate nonzero surface tension[18-23] or to mimic anisotropic growth.[15,23-29] In this respect, the role of the DLA model and its variants in understanding growth phenomena in nonequilibrium systems is considered by many authors[1-5] as being analogous to Ising models with respect to critical phenomena.

Despite the importance and the apparent simplicity of the Witten and Sander model,[6] there is still no rigorous theory for diffusion-limited growth processes. Moreover, there is no convincing experimental demonstration that well-known fractal aggregates, e.g., electrodeposition clusters or viscous fingers, actually belong to the DLA universality class. In fact, only a little is known in quantitative terms about the structure of DLA clusters. Most of the numerical analysis of growing patterns have focused on the determination of the fractal dimension.[1-3,6,11] However, the fractal dimension is a global property of the cluster and it does not provide a deep insight into the geometrical complexity of the aggregate. Only very recently,[12,30] has more attention been paid to the computation of the generalized fractal dimensions[31-34] D_q, which are closely related (by means of a Legendre transform) to the $f(\alpha)$ spectrum[35-39] of singularities of strength α (α is also called the local scaling exponent). But, thus far, the conjectured global self-similarity[6,11] of the shape of DLA patterns still remains unelucidated since recent numerical attempts[30] have failed to show that the D_q's coincide, i.e., the $f(\alpha)$ spectrum is concentrated on a simple point $\alpha=D_0$ [the local scaling exponent $\alpha(\mathbf{x})$ does not depend on $\mathbf{x}$].

Although the measurement of the D_q's and $f(\alpha)$ spectrum is without a doubt very instructive, it only provides statistical information about the scaling properties of fractals. As already emphasized in previous studies,[40,41] the $f(\alpha)$ spectrum identifies the underlying singularities and quantifies their relative contributions, but it fails to fully characterize the local self-similarity of fractals,[42] since it does not keep track of the spatial location of these

singularities. An efficient multiscale analysis is thus essential to collect additional information concerning the hierarchy which governs the spatial distribution of these singularities. A known method which comes close to satisfying this requirement is the *wavelet transform*.[43,44] This mathematical technique provides a two-dimensional unfolding for one-dimensional signals, displaying both the position and the scale as independent variables. The wavelet transform was introduced in the early 1980s in the context of seismic data analysis.[45] Since then it has been applied in many different fields: pure mathematics,[46–52] quantum mechanics,[52–54] signal analysis,[43,45,55–57] synthesis of sounds,[57] and computer vision.[58] The remarkable properties of this multiresolution decomposition method have been mainly used to provide visual access to some of the structural characteristics of a signal, e.g., detection of abrupt changes in sound signals,[55] and edge and pattern recognition.[58,59] Very recently, the wavelet transform has been compared to a mathematical microscope which is well appropriated to investigate the local self-similarity of fractal objects.[40,41,60,61] The ability of this microscope to reveal the underlying construction rules and to resolve local scaling properties through the determination of local pointwise dimensions[62] $\alpha(x)$ has been demonstrated on pedagogical examples, e.g., Weierstrass fractal functions over the real line[60] and (multi)fractal probability measures on well-known Cantor sets.[40,41,61] Further application of the wavelet analysis to the velocity field of wind tunnel turbulence at very high Reynolds numbers has provided the first visual evidence of the celebrated Richardson cascade;[63] this analysis suggests that the energy-cascading process displays multifractal properties and presents remarkable similarities with the construction rules of nonhomogeneous Cantor sets. Even more spectacular is the recent application[40,41] of the wavelet transform to multifractal invariant measures of some well-known one-dimensional dynamical systems modeling the transition to chaos observed in dissipative systems. In this context, the wavelet transform has been shown to be of fundamental interest, since it naturally reveals the renormalization operation which is essential to the theoretical understanding of the universal properties of this nonequilibrium phase transition.[41]

Our purpose here is to generalize the wavelet analysis to fractal growth phenomena.[41] Most of the theoretical activity in this field has been based on phenomenological approaches.[7–10] Many attempts to adapt real-space renormalization-group methods[64] remain unclear,[65–67] while interesting developments have been recently reported on introducing a fixed-scale transformation[68] instead of coarse graining as in the renormalization-group theory. But many important theoretical questions remain unanswered; in particular, it is still an open question whether the fractal geometry of DLA clusters is a product of the randomness in the growth process[23,69] or the result of a cascade of deterministic tip-splitting instabilities.[70–72] It is hoped that the application of the wavelet transform will allow us to resolve some of these theoretical interrogations. Our analysis will be twofold. In the present study, we extend the wavelet transform analysis to multidimensional signals[73] with the specific aim of characterizing the spatial distribution of local scaling properties of fractal aggregates embedded in a two-dimensional space. Our approach consists in focusing the wavelet microscope on the geometrical complexity of numerical and experimental fractal aggregates. A short account of some of the results of a wavelet analysis of snowflake fractals and DLA clusters has been published previously.[74] In a subsequent study,[75] we will go beyond this static analysis, since the wavelet transform can be used as well to characterize the local scaling structure of the growth probability distribution for the perimeter sites of a fractal aggregate. Recent theoretical[72,76–81] and experimental[82,83] studies have revealed the multifractal character of the growth probability distribution of Laplacian fractals. Our aim is to achieve a comprehensive study of the geometrical and dynamical properties of Laplacian growth phenomena, and to emphasize the wavelet transform as a very promising tool which might play a decisive role in the development of a unified theory of nonequilibrium growth processes.

Among the various experimental illustrations of fractal pattern forming phenomena, electrochemical metallic deposition[84] is commonly considered as the paradigm for theoretical studies of diffusion-limited aggregation. In fact, by varying the concentration of metal ions and the cathode potential, one can explore different morphologies, such as dense radial aggregates,[85] dendritic patterns,[86,87] and fractal aggregates.[86,88–90] Fractal patterns are usually obtained in the limit of small ionic concentration and small voltage. These fractal electrodeposition clusters have been extensively studied and it has been conjectured[88–90] that they are similar to Witten and Sander DLA clusters. In fact, the deep connection between highly ramified electrodeposits and DLA clusters has been explored to a limited extent both theoretically and experimentally. In a preliminary study performed in collaboration with Swinney,[91] we have developed a comparative study of zinc electrodeposition aggregates and DLA clusters grown in a strip geometry. This study was essentially based on box-counting and fixed-mass computations of the spectrum of generalized fractal dimensions. In this paper we take advantage of the capabilities of the wavelet transform to push this analysis further. In particular, we bring definite evidence for the structural self-similarity of electrodeposit aggregates and DLA clusters, which are shown to mimic remarkably the geometrical complexity of the experimental patterns. To test the robustness of our results against the nature of the metallic compound and the specific geometry in which the growth process takes place, we consider copper instead of zinc and a circular cell instead of a strip configuration. No significant quantitative modification of the geometrical properties of the electrodeposition clusters is induced by these changes in the experimental protocol.

The paper is organized as follows. In Sec. II we describe the implementation of complementary box-counting and fixed-mass algorithms devoted to the computation of the generalized fractal dimensions D_q and the $f(\alpha)$ spectrum of singularities. The wavelet transform is introduced in Sec. III with special emphasis on its ability

to characterize the local scaling properties of two-dimensional fractal aggregates. In Sec. IV we illustrate the efficiency of the wavelet microscope to reveal the construction rule of highly self-similar snowflake fractals and to capture the local self-similarity properties of multifractal aggregates. Section V is devoted to a systematic study of the structural complexity of DLA clusters. We show that DLA clusters are statistically self-similar fractals. This wavelet transform analysis suggests that DLA clusters possess a deterministic chaotic recursive structure. In Sec. VI we present a comparative analysis of two-dimensional copper electrodeposition clusters in the limit of small ionic concentration and small current. This experimental study brings quantitative evidence indicating that the electrodeposition growth mechanism is very likely to be governed by a diffusion-limited aggregation process. In Sec. VII the results are summarized and the possibility of applying the wavelet transform to other experimental situations is briefly discussed.

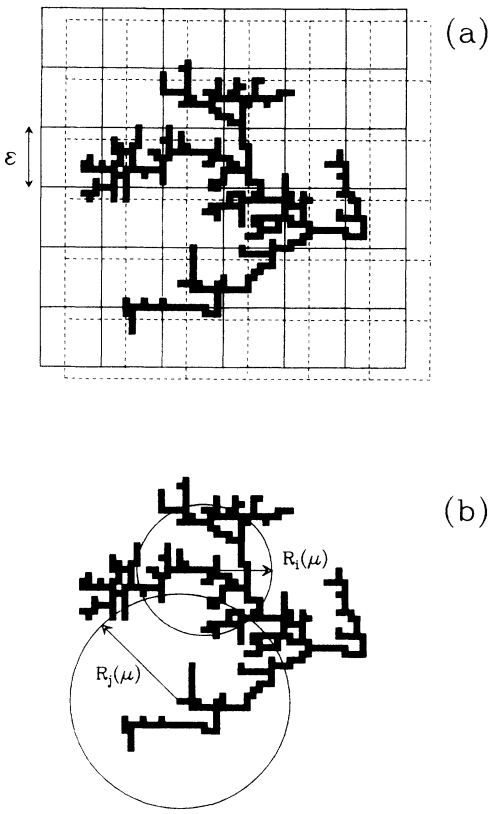

FIG. 1. (a) Illustration of the box-counting algorithm. The partition function $Z_q(\epsilon)$ [Eq. (2.1)] is computed using a grid of square boxes of size ϵ. The D_q's are estimated when averaging over randomly chosen positions of the grid with respect to the aggregate. (b) Illustration of the fixed-mass algorithm. Balls of constant mass μ are centered on randomly chosen reference points of the boundary of the aggregate. The D_q^{-1}'s are estimated from the arithmetic mean $\Xi_r(\mu)$ [Eq. (2.7)].

II. GENERALIZED FRACTAL DIMENSIONS AND SPECTRUM OF SINGULARITIES

A. Definitions

In the past decade, much effort has been devoted to the characterization of measures lying upon possibly fractal sets. In the context of dynamical systems theory, the Renyi dimensions[31] D_q have been proposed to describe the geometric and probabilistic features of strange attractors.[32–34,92] Recently these generalized fractal dimensions have been used to quantify the self-similar properties of either numerical[30,91] or experimental fractal aggregates.[91] When investigating the scaling properties of the geometry of a fractal aggregate, the measure μ is simply the mass of the object. The Renyi dimensions are closely related, by means of a Legendre transform, to the $f(\alpha)$ spectrum of singularities of the corresponding measure.[35–39] This deep connection has been recently understood using a statistical mechanics and thermodynamics formalism.[38,39,93]

For concreteness let us define a uniform square grid of size ϵ [Fig. 1(a)]. Let μ_i denote the proportion of the total mass of the object inside the ith box: for empty boxes μ_i vanishes. Then let us introduce the partition function[32,33]

$$Z_q(\epsilon)=\sum_{i=1}^{N}\mu_i^q(\epsilon)\ , \tag{2.1}$$

where $N\sim 1/\epsilon^2$ is the number of boxes of the grid. The so-called order-q generalized dimensions[31–33] are obtained from the power-law behavior of the partition function in the limit $\epsilon\to 0$ ($N\to+\infty$):

$$Z_q(\epsilon)\sim\epsilon^{(q-1)D_q}\ . \tag{2.2}$$

D_0, D_1, and D_2 are the well-known capacity, information, and (two-point) correlation dimensions.[34] As higher power q in Eq. (2.1) select denser regions, the D_q's are positive numbers whose values generally decrease with q. For globally self-similar fractals all the D_q's coincide.[93]

It is easy to connect the generalized fractal dimensions D_q to the $f(\alpha)$ spectrum of singularities.[35–39,93] In each box the measure μ increases with the size ϵ like

$$\mu_i\sim\epsilon^{\alpha_i}\ , \tag{2.3}$$

where the crowding index[38] $\alpha_i(\epsilon)$ is generally position dependent. At any fixed ϵ there exist, however, several boxes with a given crowding index, say α. Their number $N_\alpha(\epsilon)$ scales with ϵ like

$$N_\alpha(\epsilon)\sim\rho(\alpha)\epsilon^{-f(\alpha)}\ , \tag{2.4}$$

i.e., these boxes cover a subset of fractal dimension $f(\alpha)$. Substituting Eqs. (2.3) and (2.4) in Eq. (2.1), one gets

$$Z_q(\epsilon)\sim\int\epsilon^{\alpha q-f(\alpha)}\rho(\alpha)d\alpha\ , \tag{2.5}$$

where α is a quasicontinuous variable. Since ϵ is very small, the integral will be dominated by the value of α which makes the exponent minimal. This immediately yields the relation[35–39] [when $f(\alpha)$ and D_q are differentiable functions]

$$f(\alpha)=\alpha q-(q-1)D_q\ ,$$
$$\alpha(q)=\frac{d}{dq}(q-1)D_q\ . \tag{2.6}$$

Therefore, the spectrum of singularities $f(\alpha)$ and the generalized fractal dimensions D_q are connected by the Legendre transform (2.6). It has been argued[39,93] that q and $\tau(q)=(q-1)D_q$ assume for the partition function Z_q the role that the inverse temperature and the free energy have respectively in thermodynamics. In this context, the Legendre transform (2.6) indicates that the place of energy and entropy is taken by α and f, i.e., the variables conjugate to q and τ.

It is noteworthy that *uniform (globally self-similar) fractals*[38,42,93,94] correspond to the special class of fractals such that all the D_q's coincide. Thus, from Eq. (2.6), the $f(\alpha)$ spectrum of uniform fractals is concentrated on a single point $\alpha=D_0=D_q$. In contrast, *multifractals*[38,93,94] are usually characterized by a monotonic decreasing dependence of D_q versus q; hence α is no longer unique but may take on values in a finite range $[\alpha_{\min},\alpha_{\max}]$, while $f(\alpha)$ turns out to be a single humped function with D_0 as its maximum; $\alpha_{\min}=\lim_{q\to+\infty}D_q$ and $\alpha_{\max}=\lim_{q\to-\infty}D_q$ characterize the scaling properties of the most concentrated and most rarified regions of the fractal object respectively [see Eq. (2.1)].

B. Measurement of the fractal dimensions D_q

Difficulties in the actual computation of the generalized fractal dimensions D_q mainly arise from intrinsic properties of fractals, namely, lacunarity[42] and nonuniformity[38,93,94] (multifractality). Lacunarity manifests itself as intrinsic oscillations[95–99] in the usual linear regressions of the log-log procedure used to measure the D_q's and makes an accurate dimension estimate an elusive goal in many cases.[98,99] Multifractality requires the simultaneous characterization of the most concentrated ($D_{+\infty}$) and the most rarified ($D_{-\infty}$) regions on the fractal which is a rather difficult task because of poor sampling statistics. Several numerical approaches have been followed to compute the D_q's. The proposed algorithms are essentially of two kinds:[100,101] (i) box-counting[102] or *fixed-size* algorithms,[103] which are well suited to estimate the D_q's with $q\geq 0$, as long as D_0 is not too large; and (ii) nearest-neighbor or *fixed-mass*[104,105] algorithms, which are most efficient to overcome statistical fluctuations and thus can be used to estimate the D_q's with $q<0$.

1. Box-counting algorithms

The values of D_q for $q\geq 0$ are estimated with use of a box-counting algorithm. The aggregate is covered with a grid of square boxes of size ϵ, which varies from 2^{-9} to 2^0 [Fig. 1(a)]. According to the scaling behavior (2.2) of the partition function in the limit $\epsilon\to 0$, the D_q's are given from the slopes of graphs of $\ln Z_q/(q-1)$ versus $\ln\epsilon$ for small ϵ.

Two factors have proved to be crucial in obtaining robust estimates of D_q. First, since the estimates of D_q depend on the location of the grid with respect to the fractal cluster,[99,101] we average $\ln Z_q/(q-1)$ for 50 different randomly distributed locations of the origin of the grid for each value of ϵ as sketched in Fig. 1(a). Second, the boundary of the aggregate is defined by elementary cells centered at each boundary site, and the values of μ_i are calculated from the portion of area of these cells in each box of the grid.[91] The ultraviolet cutoff will thus lead to a crossover to $D_q\to 2$ at small ϵ rather than 1 (dimension of a line) or 0 (dimension of a point); this contrasts with previous studies which counted the number of points in each box.

2. Fixed-mass algorithms

For $q<0$, the values of D_q cannot be reliably determined with a box-counting algorithm because of its inefficiency in handling spurious small μ_i. However, a nearest-neighbor algorithm can be used;[104,105] this algorithm requires some averaging over fixed-mass calculations instead of fixed-size calculations inherent to the box-counting algorithms.

Let us consider a set of balls $\mathcal{B}_i(\mu)$, centered on each point of the aggregate boundary and containing a constant mass μ [Fig. 1(b)]. These balls have a radius $R_i(\mu)$. Similarly to Eq. (2.1), one can introduce the function

$$\Xi_\tau(\mu)=\frac{1}{M}\sum_{i=1}^{M}R_i(\mu)^{-\tau}\ , \tag{2.7}$$

where M is the total number of boundary sites. In the limit $\mu\to 0$, this function scales like

$$\Xi_\tau(\mu)\sim\mu^{-\tau/D_q}\ , \tag{2.8}$$

where again $\tau(q)=(q-1)D_q$. The numerical measurement of D_q^{-1} is actually performed by computing the slopes of the regression lines of the curves $-\tau^{-1}\ln\Xi_\tau(\mu)$ versus $\ln\mu$. In the implementation of the algorithm only a subset of N reference points chosen at random on the boundary of the aggregate ($N<M$) is used to compute the arithmetic mean in Eq. (2.7). Of course, large values of N must be used to obtain asymptotic estimates.

For $q<0$, $\tau(q)$ is also negative and in the limit $q\to-\infty$, the terms which dominate in the sum $\Xi_\tau(\mu)$ [Eq. (2.7)] correspond to large radii R_i which makes the estimate of $D_{-\infty}$ less sensitive to statistical fluctuations (we recall that $D_{-\infty}$ characterize the region where the measure μ is the most rarified). However, in return, the most concentrated regions correspond to small radii R_i, which makes the estimate of D_q in the limit $q\to+\infty$ much less reliable than the estimate derived when using the fixed-size partition defined in Eq. (2.1).

C. Measurement of the $f(\alpha)$ spectrum of singularities

In previous studies, the D_q's were usually determined from box-counting or fixed-mass algorithms and the $f(\alpha)$ curve was naturally deduced from the Legendre transform (2.6) of the curve $\tau(q)=(q-1)D_q$. But such a computation requires first a smoothing of the D_q curve and

then Legendre transforming. This procedure has a main disadvantage: The smoothing operation prevents the observation of any singularities in the curves $f(\alpha)$ or $\tau(q)$, and the interesting physics of phase transitions in the scaling properties of the fractal measure can be completely missed.[100]

Several methods[98,100,105,106] have been recently proposed for the direct computation of the $f(\alpha)$ spectrum based on log-log plots of the quantities in Eqs. (2.3) and (2.4). Unfortunately, the application of these methods suffers from neglected logarithmic corrections[106–108] which arise from the scale-dependent prefactors in Eq. (2.4). To overcome these difficulties we usually employ the following trick.[101] Let us derive the partition function $Z_q(\epsilon)$ [Eq. (2.1)] with respect to q:

$$\frac{d}{dq}Z_q(\epsilon)=\sum_{i=1}^{N}\mu_i^q(\epsilon)\ln\mu_i(\epsilon)\ . \tag{2.9}$$

From Eq. (2.2) and the definition of $\alpha(q)$ in Eq. (2.6), one deduces

$$\alpha(q)=\frac{d}{dq}(q-1)D_q$$
$$=\lim_{\epsilon\to 0}\frac{1}{\ln\epsilon}\sum_i\tilde{\mu}_i(q,\epsilon)\ln\mu_i(\epsilon)\ , \tag{2.10}$$

where

$$\tilde{\mu}_i(q,\epsilon)=\mu_i^q(\epsilon)\Big/\sum_j\mu_j^q(\epsilon)\ . \tag{2.11}$$

Then upon using the definition of $f=\alpha q-(q-1)D_q$ in Eq. (2.6), one gets

$$f(\alpha(q))=\lim_{\epsilon\to 0}\frac{1}{\ln\epsilon}\sum_i\tilde{\mu}_i(q,\epsilon)\ln\tilde{\mu}_i(q,\epsilon)\ . \tag{2.12}$$

Therefore, the singularity spectrum can be directly computed from Eqs. (2.10) and (2.12) without explicitly Legendre transforming, without suffering from poor sampling statistics for large and small values of α, and without neglecting logarithmic corrections. In a recent work by Chhabra and Jensen,[108] this alternative definition of $f(\alpha)$ has been proved to be the Hausdorff dimension of the measure theoretic support of $\tilde{\mu}(q)$, while $\alpha(q)$ is an average singularity strength. Consequently, evaluating the singularity spectrum from Eqs. (2.10) and (2.12) resolves the mathematical ambiguities inherent to most of the numerical methods, which computes f as a box dimension [Eq. (2.4)] rather than a Hausdorff dimension.[38,39]

III. WAVELET TRANSFORM OF FRACTALS

A. Wavelet transforms associated to the affine group

1. Definitions

The wavelet transform is a technique which consists in decomposing an arbitrary signal $f(t)$, into elementary contributions, the so-called *wavelets* which are constructed from one single function g by means of dilations and translations:[43,44,52]

$$g_{a,b}(t)=\mathcal{A}(a,b)g(t)$$
$$=a^{-1/2}g(a^{-1}(t-b)),\quad t\in\mathbb{R}\ , \tag{3.1}$$

where the parameters a and b can be chosen to vary continuously ($a,b\in\mathbb{R}$, $a>0$), or to be restricted to a discrete lattice. The operator $\mathcal{A}(a,b)$ represents the action of the affine group. The wavelet transform is generally a complex-valued function which is given by

$$T_g(a,b)=a^{-1/2}C_g^{-1/2}\int dt\, g^*(a^{-1}(t-b))f(t)\ , \tag{3.2}$$

where the asterisk denotes the complex conjugate. Expressing Eq. (3.2) in terms of Fourier transforms one gets

$$T_g(a,b)=a^{1/2}C_g^{-1/2}\int d\omega\, e^{i\omega b}\hat{g}^*(a\omega)\hat{f}(\omega)\ , \tag{3.3}$$

where the Fourier transform of a function $f(t)$ is defined by

$$\hat{f}(\omega)=(2\pi)^{-1/2}\int dt\, e^{i\omega t}f(t)\ .$$

From Eqs. (3.2) and (3.3), it is clear that the wavelet transform provides a time-frequency (space-scale) analysis of the signal $f(t)$ with filter $\hat{g}(a\omega)$ of constant relative resolution $\Delta\omega/\omega=$const. The function g is called *analyzing wavelet* if it satisfies the *admissibility condition*:[43,46,52]

$$C_g=2\pi\int d\omega|\hat{g}(\omega)|^2/\omega<\infty\ . \tag{3.4}$$

For wavelets $g\in L^2(\mathbb{R},dx)\cap L^1(\mathbb{R},dx)$, this condition essentially means that $g(t)$ is of zero mean:

$$\int dt\, g(t)=0\ . \tag{3.5}$$

Then the wavelet transform is an isometry and one can reconstruct the original function from the inversion formula[43,46,52]

$$f(t)=C_g^{-1/2}\int\int a^{-2}da\,db\,T_g(a,b)g_{a,b}(t)\ , \tag{3.6}$$

where $a\in\mathbb{R}^+$, $b\in\mathbb{R}$, and $a^{-2}da\,db$ is the natural surface element in the (a,b) half-plane that does not change under shifts and rescalings.

In this section, we have supposed that the signal $f(t)$ is square integrable, i.e., of finite energy: $\int dt|f(t)|^2<\infty$. The wavelet transform is thus a linear transformation which preserves energy:

$$\int dt|f(t)|^2=\int a^{-2}da\,db|T_g(a,b)|^2\ . \tag{3.7}$$

2. Some examples of analyzing wavelets

The Morlet wavelets: An historical example of analyzing wavelets can be found in the pioneering work of Morlet and collaborators.[45] These wavelets are defined as superpositions of shifted Gaussians in frequency space. For every $\Omega\in\mathbb{R}$, the function

$$\hat{g}_\Omega(\omega)=e^{-(\omega-\Omega)^2/2}-e^{-\Omega^2/4}e^{-(\omega-\Omega)^2/4} \tag{3.8}$$

satisfies $\hat{g}_\Omega(0)=0$. Its inverse Fourier transform is thus an admissible wavelet:

$$g_\Omega(t)=e^{i\Omega t}(e^{-t^2/2}-\sqrt{2}e^{-\Omega^2/4}e^{-t^2})\ . \tag{3.9}$$

This one-parameter family of analyzing wavelets is usually called the Morlet wavelets.[45] Let us note that, if Ω is chosen sufficiently large, then the second (counter) terms in Eqs. (3.8) and (3.9) become negligible.

The Mexican hat. A very popular analyzing wavelet is the so-called Mexican hat,[44] i.e., the second derivative of the Gaussian function:

$$g(t)=(1-t^2)e^{-t^2/2} . \tag{3.10}$$

Its Fourier transform obviously vanishes for $\omega=0$:

$$\hat{g}(\omega)=\omega^2 e^{-\omega^2/2} . \tag{3.11}$$

This admissible wavelet is well localized in both direct and Fourier spaces. It will be commonly used in the remainder of this paper. The Mexican hat (3.10) is sketched in Fig. 2(a).

Piecewise constant wavelets. Fast discrete wavelet transform algorithms have been recently implemented by computer.[101,109] These algorithms require a piecewise constant (or piecewise linear) wavelets. In previous studies[40,41,61,63] we have sometimes used the piecewise constant approximation of the Mexican hat:

$$g(t)=\begin{cases} 1, & |t|<1 \\ -\frac{1}{2}, & 1<|t|<3 \\ 0, & |t|>3 . \end{cases} \tag{3.12}$$

B. Wavelet transforms associated with the d-dimensional Euclidean group with dilations

1. Definitions

When one intends to generalize to more than one dimension the whole machinery developed for the $ax+b$ affine group (Sec. III A), it is natural to consider the d-dimensional Euclidean group with dilations.[73,110] This group is a nonunimodular locally compact group. $\Omega(a,r,\mathbf{b})$ defined below is its most natural unitary representation in $L^2(\mathbb{R}^d,d^dx)$, which turns out to be both irreducible and square integrable:

$$g_{a,r,\mathbf{b}}(\mathbf{x})=\Omega(a,r,\mathbf{b})g(\mathbf{x}) =a^{-d/2}g(a^{-1}r^{-1}(\mathbf{x}-\mathbf{b})) , \tag{3.13}$$

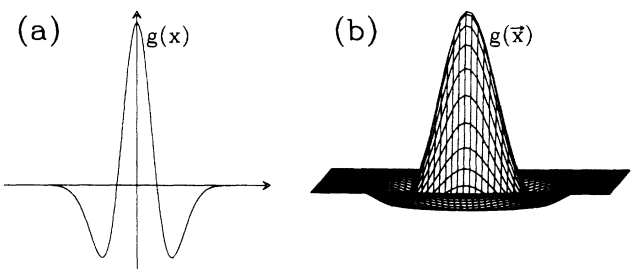

FIG. 2. The Mexican hat analyzing wavelet. (a) The one-dimensional variant defined in Eq. (3.10). (b) The radial two-dimensional variant defined in Eq. (3.23).

where a, r, and $\mathbf{b}$ are, respectively, the dilation parameter ($a>0$), the d-dimensional rotation operator [$\Re^r g(\mathbf{x})=g(r^{-1}\mathbf{x})$], and the displacement vector. The wavelet transform is defined as follows:

$$T_g(a,r,\mathbf{b})=a^{-d/2}C_g^{-1/2}\int d^dx\, g^*(a^{-1}r^{-1}(\mathbf{x}-\mathbf{b}))f(\mathbf{x}) . \tag{3.14}$$

In the Fourier space, Eq. (3.14) is written as

$$T_g(a,r,\mathbf{b})=a^{d/2}C_g^{-1/2}\int d^dk\, e^{i\mathbf{k}\mathbf{b}}\hat{g}^*(ar^{-1}\mathbf{k})\hat{f}(\mathbf{k}) , \tag{3.15}$$

where the Fourier transform of a function $f(\mathbf{x})$ is defined by

$$\hat{f}(\mathbf{k})=(2\pi)^{-d/2}\int d^dx\, e^{-i\mathbf{k}\mathbf{x}}f(\mathbf{x}) .$$

For the wavelet transform to be invertible, the wavelet $g(\mathbf{x})$ must satisfy the admissibility condition

$$C_g=(2\pi)^d\int d^dk\,|\hat{g}(\mathbf{k})|^2/|\mathbf{k}|^d<\infty . \tag{3.16}$$

The reconstruction formula can be written as

$$f(\mathbf{x})=C_g^{-1/2}\int\int\int a^{-(d+1)}da\,dr\,d^db \times T_g(a,r,\mathbf{b})g_{a,r,\mathbf{b}}(\mathbf{x}) , \tag{3.17}$$

where $a^{-(d+1)}da\,dr\,d^db$ is the left Haar measure and dr the Haar measure on SO(d) (the special orthogonal group in d dimension). The energy conservation formula becomes

$$\int\int\int d^dx\,|f(\mathbf{x})|^2 =\int\int\int a^{-(d+1)}da\,dr\,d^db\,|T_g(a,r,\mathbf{b})|^2 . \tag{3.18}$$

2. Some examples of analyzing wavelets

The d-dimensional Morlet wavelet:[73] The d-dimensional Morlet wavelet is defined as follows:

$$g_{\mathbf{q},A}(\mathbf{x})=e^{i\mathbf{q}\mathbf{x}}(e^{-\langle\mathbf{x}|A\mathbf{x}\rangle/2}-e^{-\langle\mathbf{q}|B\mathbf{q}\rangle/2}e^{-\langle\mathbf{x}|A\mathbf{x}\rangle/2}) . \tag{3.19}$$

Its Fourier transform takes the form

$$\hat{g}_{\mathbf{q},A}(\mathbf{k})=|\det B|^{1/2}(e^{-\langle(\mathbf{k}-\mathbf{q})|B(\mathbf{k}-\mathbf{q})\rangle/2} -e^{-\langle\mathbf{q}|B\mathbf{q}\rangle/2}e^{-\langle\mathbf{k}|B\mathbf{k}\rangle/2}) . \tag{3.20}$$

A is a positive definite matrix ($\langle\mathbf{x}|A\mathbf{x}\rangle>0$), and $B=A^{-1}$. The counterterms in $g_{\mathbf{q},A}$ and $\hat{g}_{\mathbf{q},A}$ guarantee that $\hat{g}_{\mathbf{q},A}(0)=0$, i.e., the admissibility condition (3.16) is fulfilled. In practice, $\mathbf{q}$ is chosen in such a way that the counterterms in Eqs. (3.19) and (3.20) are negligible.

The d-dimensional Mexican hat.[73] The d-dimensional Mexican hat is defined by

$$g_A(\mathbf{x})=(d-\langle\mathbf{x}|A\mathbf{x}\rangle)e^{-\langle\mathbf{x}|A\mathbf{x}\rangle/2} , \tag{3.21}$$

whose Fourier transform is

$$\hat{g}_A(\mathbf{k})=|\det B|^{1/2}\langle\mathbf{k}|B\mathbf{k}\rangle e^{-\langle\mathbf{k}|B\mathbf{k}\rangle/2} , \tag{3.22}$$

where A is a positive definite matrix and $B=A^{-1}$. For the particular choice $A=B=I$, one recovers in the $d=2$ dimension the so-called radial Mexican hat,[41,74] which is illustrated in Fig. 2(b):

$$g(\mathbf{x})=(2-|\mathbf{x}|^2)e^{-|\mathbf{x}|^2/2}\ ; \tag{3.23}$$

its Fourier transform writes

$$g(\mathbf{k})=|\mathbf{k}|^2 e^{-|\mathbf{k}|^2/2}\ . \tag{3.24}$$

The French top hat. A natural generalization in $d=2$ dimensions of the piecewise constant wavelet defined in Eq. (3.12) is the French top hat:

$$g(\mathbf{x})=\begin{cases}1, & |x|,|y|<1\\ -\frac{1}{8}, & 1<|x|,|y|<3\\ 0, & |x|,|y|>3\ .\end{cases} \tag{3.25}$$

In our analysis of fractal aggregates, we will mainly use the top hat wavelet to achieve a fast but systematic investigation of the scaling properties of the considered aggregates. Then we will use the radial Mexican hat to obtain final results.

C. Wavelets and scalings of fractal aggregates

As pointed out in Sec. II A, a typical property of fractals is that they are self-similar at small length scales.[42] Local self-similarity means that the fractal measure[92] μ (e.g., the mass of the aggregate) scales around the point $\mathbf{x}_0$ as [Eq. (2.3)]

$$\mu(\mathcal{B}(\mathbf{x}_0,\lambda\epsilon))\sim\lambda^{\alpha(\mathbf{x}_0)}\mu(\mathcal{B}(\mathbf{x}_0,\epsilon))\ , \tag{3.26}$$

where $\mathcal{B}(\mathbf{x}_0,\epsilon)$ is an ϵ ball centered at $\mathbf{x}_0$ and $\alpha(\mathbf{x}_0)$ is the local scaling exponent (Refs. 38, 42, 62, 100, and 106). As previously mentioned, the D_q's and the $f(\alpha)$ spectrum provide only statistical information about the spectrum of α values over the whole aggregate. To collect additional information on the spatial location of these singularities, let us generalize the wavelet transform analysis developed in Refs. 40, 41, and 61 to fractal measures over $\mathbb{R}^d$.

Let g be an analyzing wavelet over $\mathbb{R}^d$ that is localized around the origin and some of whose moments are zero. We define the wavelet transform of the measure μ with respect to the wavelet g as[74]

$$T_g(a,r,\mathbf{b})=\int d\mu(\mathbf{x})g^*(a^{-1}r^{-1}(\mathbf{x}-\mathbf{b}))\ , \tag{3.27}$$

where for the sake of simplicity we have neglected any normalization factor in front of the integral [see Eq. (3.14)]. Then for noninteger scaling exponent $\alpha(\mathbf{x}_0)$ and a wavelet which decays sufficiently fast at infinity,[60,101,111] the local scaling behavior of μ [Eq. (3.26)] is mirrored by the wavelet transform

$$\begin{aligned}T_g(\lambda a,\mathbf{x}_0+\lambda\mathbf{b})&=\int d\mu_{\mathbf{x}_0}(\mathbf{x})g^*((\lambda a)^{-1}r^{-1}(\mathbf{x}-\lambda\mathbf{b}))\ ,\\ &=\int d\mu_{\mathbf{x}_0}(\lambda\mathbf{y})g^*(a^{-1}r^{-1}(\mathbf{y}-\mathbf{b}))\ ,\end{aligned}$$

which scales, in the limit $\lambda\to 0$ like

$$T_g(\lambda a,\mathbf{x}_0+\lambda\mathbf{b})\sim\lambda^{\alpha(\mathbf{x}_0)}T_g(a,\mathbf{x}_0+\mathbf{b})\ , \tag{3.28}$$

i.e., with the same exponent $\alpha(\mathbf{x}_0)$ as μ. For integer exponents, the singularities may be masked by polynomial behaviors;[101] in order to overcome this practical difficulty, one generally considers wavelets that operate modulo some polynomials.

At that point, let us mention that on the basis of usual pointwise dimension calculations[62] [Eq. (2.3)] we have disregarded anisotropic effects in the local scaling behavior of the measure under consideration [Eqs. (3.26) and (3.28)]. Henceforth, we will skip, in the wavelet transform notation, the straightforward integration over the angular variables. From Eq. (3.28) the wavelet transform can be seen as a "mathematical microscope" whose position and magnification are $\mathbf{x}_0$ and a^{-1}, respectively, and whose optics is given by the choice of the analyzing wavelet g. This microscope[40,41,61] allows us (i) to locate the singularities of μ (every local singularity of μ produces a conelike structure in the wavelet transform pointing toward the point $\mathbf{x}_0$ when the magnification parameter a^{-1} is increased); (ii) to estimate the strength of the singularities of μ [every singularity of μ manifests itself through a power-law behavior of $T_g(a,\mathbf{b})$ in the limit $a\to 0$, whose exponent $\alpha(\mathbf{x}_0)$ is the strength of the singularity located at $\mathbf{x}_0$]. This analogy with a mathematical microscope is apparent in the case of interest here, i.e., $\mathbb{R}^2$, where

$$r=\begin{pmatrix}\cos\theta & -\sin\theta\\ \sin\theta & \cos\theta\end{pmatrix}$$

and θ is the rotation parameter. Let us note that the radial symmetry of the analyzing wavelet g conditions the isotropy of this microscope. The possibility of using nonradial wavelets looks, however, very attractive for the study of fractals that do not scale isotropically.[100]

In the following sections, we will mainly focus on the study of the geometric properties of two-dimensional fractal aggregates. Henceforth, the probability measure μ will correspond to the mass distribution of these aggregates over the plane. We will use the radial Mexican hat [Eq. (3.23)] shown in Fig. 2(b) as analyzing wavelet. We will compute the wavelet transform in Fourier space in order to take advantage of the rapidity of the fast-Fourier-transform algorithms[101] (resolution 512×512). Despite the isotropy working hypothesis, the wavelet transform $T_g(a,\mathbf{b})$ will still depend upon three parameters a, b_x, and b_y. Because it turns out to be the most suggestive, we will adopt the following representation: For a given value of the magnification a^{-1}, we will illustrate the spatial dependence of T_g versus $\mathbf{b}$ using a three-dimensional representation; then we will visit smaller and smaller length scales showing several pictures corresponding to successively increasing values of the magnification.

IV. WAVELET TRANSFORM OF SELF-SIMILAR AND MULTIFRACTAL SNOWFLAKE PATTERNS

A. One-scale snowflake patterns

Dendritic crystal growth[112] enters the wide class of pattern formation in a diffusion field.[1–5] In contrast to

the irregularly branched structure of DLA patterns, which will be studied in Sec. V, dendritic crystals have a well-organized branched geometry, such as those seen in snowflake patterns.[113,114] It has been argued that the main difference comes from the existence of crystalline anisotropy.[1-5] In Figs. 3–6 we study a snowflake fractal which is commonly thought of as a paradigm for self-similar fractal aggregates.[115] Its construction rule [Fig. 4(a)] can be considered as a deterministic model for aggregation processes. The "seed" configuration ("basic motif") is a symmetric cross built by five particles ($n=1$). The configuration at the nth stage is obtained by adding to the four corners of the $(n-1)$-stage configuration, the cluster corresponding to the $(n-1)$th stage. Therefore, from one stage to the next stage of the construction, the cluster length size increases by a factor $l^{-1}=3$, while the number of motifs is multiplied by a factor $m=5$.

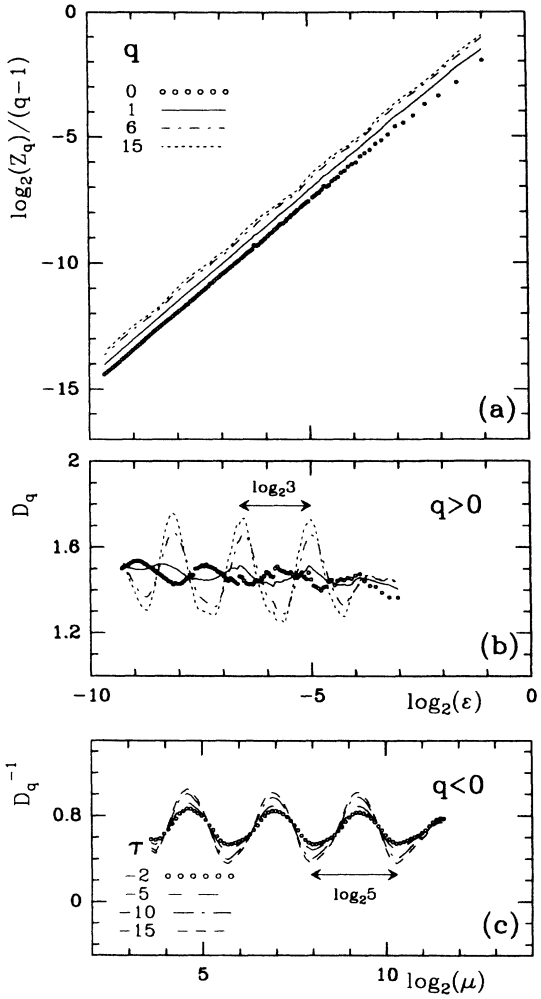

FIG. 3. These graphs illustrate the determination of the generalized fractal dimensions D_q for the one-scale snowflake fractal shown in Fig. 4(a). (a) Box-counting computation of D_q for $q \geq 0$. (b) The local dimensions D_q, given by the local slopes of the curves in (a) obtained from linear regression fits for the range $\Delta \log_2 \epsilon = 1$. (c) The local dimensions D_q^{-1} for $q<0$, obtained from local linear regression fits using fixed-mass computation ($\Delta \log_2 \mu = 1$). N.B.: We keep the notation ln in the text and $\log_2$ in the figure captions.

1. *Generalized fractal dimensions and $f(\alpha)$ spectrum*

If a measure possesses an exact recursive structure, one can compute the generalized fractal dimensions D_q using the following partition function:[38]

$$\Gamma(q,\tau,l)=\sum_{i=1}^{m} p_i^q / l_i^{\tau} , \tag{4.1}$$

where the construction rule consists in dividing a single object of size 1 and measure 1 into m identical pieces with size l_i ($l=\max l_i$) and measure p_i. At the next stage, each piece is further divided into m pieces, each with a measure reduced by a factor p_j and size by a factor l_j. At this level the partition function will be

$$\Gamma(q,\tau,l^2)=\Gamma(q,\tau,l)^2 . \tag{4.2}$$

As pointed out in Ref. 38, for such measures the first partition function $\Gamma(q,\tau,l)$ in Eq. (4.1), will generate all the others. In the spirit of the original definition of Hausdorff,[38,42] the fractal dimensions are obtained on requiring the partition function to be of the order unity. From Eq. (4.2), one deduces that the $D_q=\tau(q)/(q-1)$ are easily determined by solving

$$\Gamma(q,\tau,l)=1 . \tag{4.3}$$

As far as the one-scale snowflake fractal shown in Fig. 4(a) is concerned, the l_i are all equal to $l=\frac{1}{3}$, while the $m=5$ pieces at the first generation have the same mass and thus receive the same measure $p=\frac{1}{5}$. Thus from Eq. (4.3), we require

$$5\left[\frac{(\frac{1}{5})^q}{(\frac{1}{3})^{\tau}}\right]=1 ,$$

which yields $\tau(q)=(q-1)(\ln 5/\ln 3)$ or

$$D_q=\ln 5/\ln 3, \quad \forall q . \tag{4.4}$$

By Legendre transforming $\tau(q)$ according to Eq. (2.6), one quantifies the self-similarity of the one-scale snowflake fractal into a single scaling index $\alpha=\ln 5/\ln 3$ with the density $f(\alpha=\ln 5/\ln 3)=\ln 5/\ln 3$.

In Fig. 3, we have computed the D_q's using the fixed-size and fixed-mass algorithms described in Secs. II B 1 and II B 2, respectively. The determination of D_q for $q \geq 0$ from slopes of graphs of $\ln Z_q/(q-1)$ versus $\ln\epsilon$ [Eq. (2.2)], is illustrated in Figs. 3(a) and 3(b). These graphs are well approximated by a straight-line of slope $D_q=\ln 5/\ln 3$. However, there are regular oscillations about this line which can be interpreted as first corrections to the leading-order term $\tau(q)\ln\epsilon$ in the expansion of $\ln Z_q(\epsilon)$:

$$\ln Z_q(\epsilon)=(q-1)D_q \ln\epsilon+\Psi_q(\ln\epsilon) , \tag{4.5}$$

where Ψ_q is a periodic function of period $\ln l^{-1}=\ln 3$. These periodic oscillations are enhanced when plotting the local slope of these graphs versus $\ln\epsilon$ as shown in Fig.

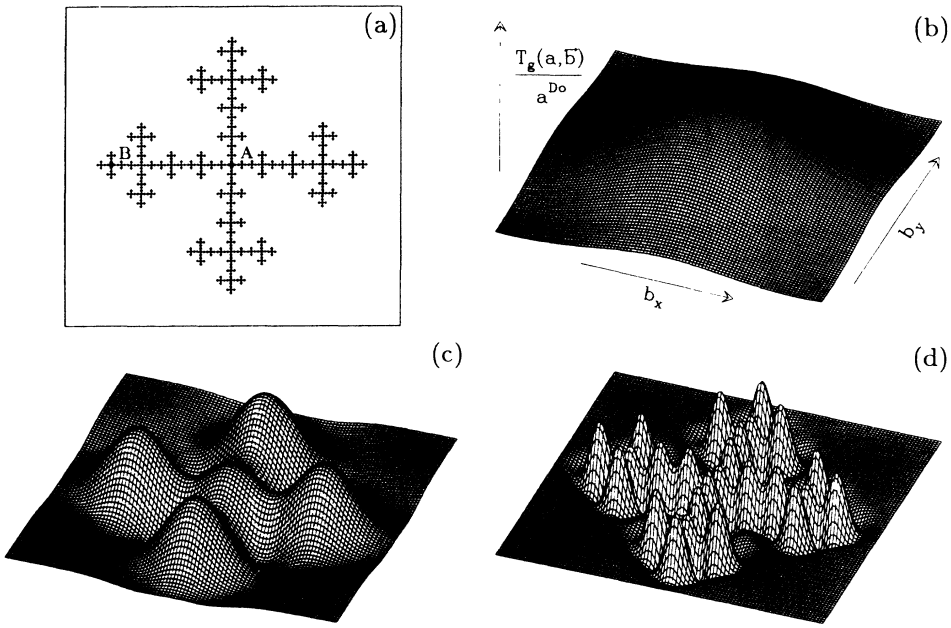

FIG. 4. Wavelet transforms of the one-scale snowflake fractals shown in (a). The analyzing wavelet is the radial Mexican hat defined in Eq. (3.23). The scale parameter a is successively divided by the same factor $l^{-1}=3$: (b) $a=a^*$, (c) $a^*/3$, and (d) $a^*/3^2$. $T_g(a,\mathbf{b})$ is expressed in a^{D_0} units, where $D_0=\log_2 5/\log_2 3$, in order to reveal the global self-similarity of the geometry of one-scale snowflake patterns (singularities of unique strength $\alpha=\log_2 5/\log_2 3$).

3(b). As previously emphasized by many authors,[95-99] these oscillations are intrinsic to lacunar fractals. A reliable estimate of the D_q's thus requires one to perform the linear regression fit on a range of scales, which is large compared to the period of these oscillations.

For $q<0$, the D_q are extracted from slopes of graphs of $-\tau^{-1}\ln\Xi_\tau(\mu)$ versus $\ln\mu$ [Eq. (2.8)] which actually yield ${D_q}^{-1}$. As shown in Fig. 3(c), there still are oscillations around a value ${D_q}^{-1}=\ln 3/\ln 5$, in good agreement with the theoretical prediction [Eq. (4.4)]. But now the period of the oscillations is $\ln m=\ln 5$ since the fixed-mass algorithm consists in partitioning the mass and not the size as in box-counting computations.

2. *Wavelet transforms*

In Figs. 4(b)–4(d), we present an overview[74] of the wavelet transform of the snowflake fractal shown in Fig. 4(a), when increasing the magnification factor a^{-1}. The analyzing wavelet is the radial Mexican hat defined in Eq. (3.23). We actually represent the spatial dependence of $\Upsilon_g(a,\mathbf{b})=a^{-\ln 5/\ln 3}T_g(a,\mathbf{b})$ for different values of the scale parameter $a=a^*$ [Fig. 4(b)], $a^*/3$ [Fig. 4(c)], and $a^*/3^2$ [Fig. 4(d)]. From a visual inspection one can convince oneself that besides the edge detection ability of the wavelet transform,[58] $\Upsilon_g(a,\mathbf{b})$ does not depend on the scaling parameter a wherever one points the wavelet microscope at the snowflake. When investigating smaller and smaller scales, the wavelet transform reveals the construction rule of the snowflake. The laser prints in Fig. 5, where $T_g(a,\mathbf{b})$ is coded using 32 shades from white

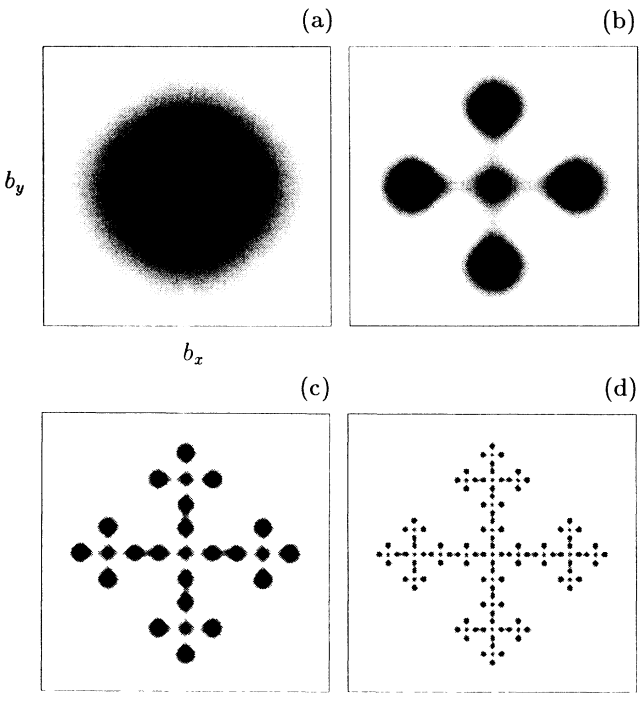

FIG. 5. Wavelet transforms of the one-scale snowflake fractal shown in Fig. 4(a). $T_g(a,\mathbf{b})$ is coded using 32 shades from white ($T_g\le 0$) to black ($\max T_g>0$) for each value of the scale parameter (a) $a=a^*$, (b) $a^*/3$, (c) $a^*/3^2$ and, (d) $a^*/3^3$. The analyzing wavelet is defined in Eq. (3.23).

$[T_g(a,\mathbf{b}) \leq 0]$ to black $[\max T_g(a,\mathbf{b}) > 0]$, bring a very attractive illustration of this fact. At large scales, one starts with a single object (let us say, a square), of length size a^* [Fig. 5 (a)]. In the next step, this object is divided into nine identical pieces, each of which is a reduced version of the original object, with length scale $a^*/3$; we remove four among the nine pieces, keeping the central piece together with the four pieces at each corner [Fig. 5(b)]. Then the same procedure is repeated in the next step for each of the five remaining pieces [Fig. 5(c)]. The snowflake is then obtained by applying the same rule subsequently [Fig. 5(d)] *ad infinitum*. In the limit $a \to 0$, the conelike structure of the wavelet transform provides a better and better approximation of the shape of the snowflake.

At each point of the aggregate, $T_g(a,\mathbf{b})$ displays a power-law behavior with exponent α independent of $\mathbf{b}$ $[\Upsilon_g(a,\mathbf{b}) \sim \text{const}]$. The measurement of this exponent at different points of the cluster is shown in Fig. 6, where $T_g(a,\mathbf{b})$ is plotted versus a in a ln-ln scale representation. Disregarding finite-size effects which occasionally affect the wavelet transform at large scales, $T_g(a,\mathbf{b})$ provides a very accurate estimate of the exponent $\alpha = \ln 5/\ln 3$, in good agreement with the theoretical prediction [Eq. (4.4)]. In fact, the scaling exponent is found to be unique, as expected for globally self-similar fractals. As indicated in Fig. 6, $T_g(a,\mathbf{b})$ actually displays an oscillatory power-law decrease in the limit $a \to 0$. The period of oscillation around the straight line in the log-log plot is $P = \ln l^{-1} = \ln 3$; this observation brings further evidence that the one-scale snowflake fractal is invariant under dilation of the length scales by a factor $l^{-1} = 3$. At this point, let us note that similar oscillations have been observed in the wavelet transform of lacunar fractals;[40,41,61] e.g., the triadic Cantor set. However, contrary to the oscillations encountered in the log-log procedure of fixed-size and fixed-mass computations of the D_q's, the existence of oscillations in the wavelet transform does not necessarily mean that the support of the measure is lacunar.[116]

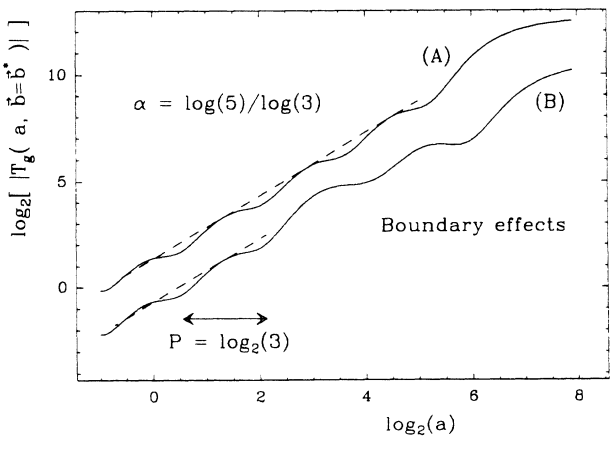

FIG. 6. Wavelet transforms of the one-scale snowflake fractal shown in Fig. 4(a). $\log_2|T_g(a,\mathbf{b}=\mathbf{b}^*)|$ vs $\log_2 a$ (arbitrary scales). The two curves correspond to the points $A(\mathbf{b}^*=\mathbf{b}_A)$ and $B(\mathbf{b}^*=\mathbf{b}_B)$ respectively defined in Fig. 4(a). The gap separating the two curves is arbitrary. The dashed lines correspond to the theoretical prediction $\alpha = \ln 5/\ln 3$. The analyzing wavelet is defined in Eq. (3.23).

B. Two-scale snowflake patterns

1. *Generalized fractal dimensions and $f(\alpha)$ spectrum*

The main difference between the construction of multiscale and one-scale fractals is the fact that the starting object is now divided into m parts, which are not all identical. However, all of these are reduced (by scaling factors that are not identical) versions of the original object. In Figs. 7–10 we extend our study to the two-scale snowflake fractal shown in Fig. 8(a). The configuration at the nth stage is obtained by adding the configuration at the $(n-1)$th stage of the growth to the four corners of the twice enlarged version of the cluster corresponding to the $(n-1)$th-stage configuration. In the spirit of the dimension calculation carried out in Sec. IV A 1, the construction rule of this snowflake consists in dividing a single object of size 1 and measure 1 into $m_1 = 4$ identical pieces with size $l_1 = \frac{1}{4}$ (S for small) and measure $p_1 = \frac{1}{8}$, and $m_2 = 1$ piece with size $l_2 = \frac{1}{2}$ (L for large) and measure $p_2 = \frac{1}{2}$. At the next stage of the construction, the same process is applied to each of these $m = m_1 + m_2 = 5$ pieces. The procedure is then repeated again and again.

Since the corresponding measure has an exact recursive structure, one can compute the generalized fractal dimensions using the partition function (4.1) and the relations (4.2) and (4.3) (with $l = l_2 > l_1$):

$$\Gamma(q,\tau,l_2) = m_1 \frac{p_1^q}{l_1^\tau} + m_2 \frac{p_2^q}{l_2^\tau} = 1 \ . \tag{4.6}$$

In Fig. 7(b) we show $D_q = \tau(q)/(q-1)$ as a function of q, as obtained numerically by solving Eq. (4.6) which is equivalent to

$$2^{-q} 4^{(1+\tau-q)} + 2^{\tau-q} = 1 \ . \tag{4.7}$$

To compute the $f(\alpha)$ spectrum one can reproduce the calculation developed in Ref. 38 for the two-scale Cantor set. At the nth level of the construction, Eq. (4.2) becomes

$$\Gamma(q,\tau,l_2^n) = \sum_j C_n^j 4^j p_1^{jq} p_2^{(n-j)q} (l_1^j l_2^{n-j})^{-\tau} = 1 \ , \tag{4.8}$$

where $C_n^j = n!/j!(n-j)!$. In the limit $n \to +\infty$, we expect that the largest term in this sum should dominate. To find the largest term we compute

$$\frac{\partial}{\partial j} \ln \Gamma(q,\tau,l_2^n) = 0 \ , \tag{4.9}$$

which is equivalent to

$$\tau = \frac{\ln(n/j-1) + \ln 4 + q \ln(p_1/p_2)}{\ln(l_1/l_2)} \ . \tag{4.10}$$

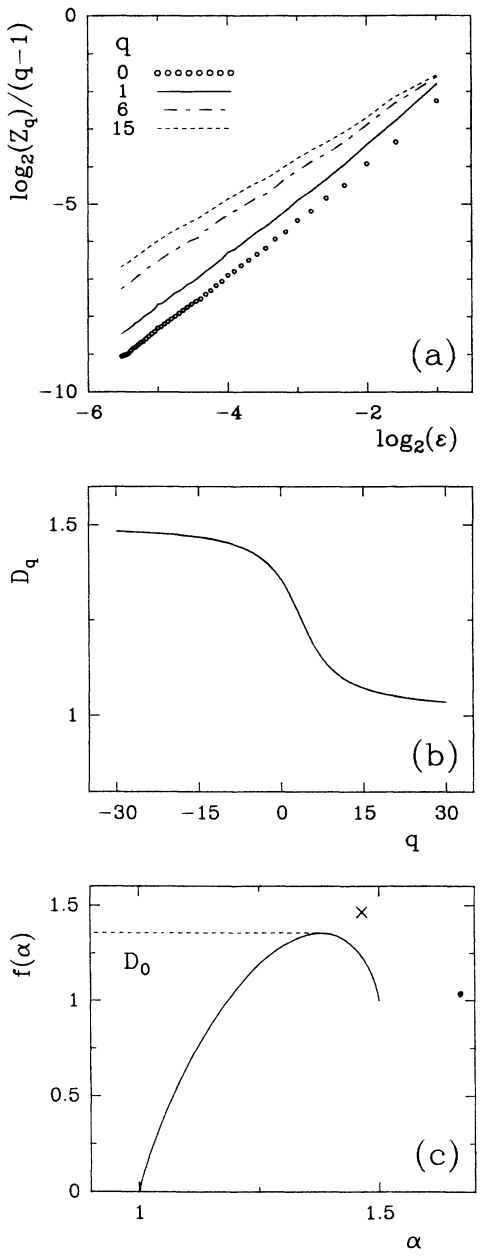

FIG. 7. These graphs illustrate the determination of the generalized fractal dimensions D_q and the $f(\alpha)$ spectrum for the two-scale snowflake fractal shown in Fig. 8(a). (a) Box-counting computation of D_q, for $q \geq 0$. (b) D_q vs q as obtained by solving Eq. (4.7). (c) $f(\alpha)$ vs α from Eqs. (4.11), (4.13), and (4.15). The $\times$ corresponds to the $f(\alpha)$ spectrum [Eq. (4.4)] of the one-scale snowflake fractal shown in Fig. 4(a).

Since we expect that the maximal term dominates the sum in Eq. (4.8), one can set this term equal to unity; after some algebraic manipulations involving Eq. (4.10), one finds

$$\ln(n/j)\ln(l_1/l_2)-\ln(n/j-1)\ln l_1 = \ln 4 \ln l_2 + q[\ln p_1 \ln l_2 - \ln p_2 \ln l_1] . \quad (4.11)$$

Thus, for any given q there will be a value of n/j which solves Eq. (4.11) and, in turn, determines $\tau(q)$ (and consequently D_q) from Eq. (4.10). This maximal term which yields τ actually comes form a set of C_n^j objects of the same size $l_1^j l_2^{(n-j)}$, where j and $n-j$ are, respectively, the number of S's and L's in the symbolic sequences that address each of these objects. Their density exponent f is determined by [see Eq. (2.4)]

$$C_n^j 4^j (l_1^j l_2^{(n-j)})^f = 1 , \quad (4.12)$$

or

$$f = \frac{(n/j-1)\ln(n/j-1)-(n/j)\ln(n/j)-\ln 4}{\ln l_1+(n/j-1)\ln l_2} . \quad (4.13)$$

The singularity exponent α is then obtained by solving [see Eq. (2.3)]

$$p_1^j p_2^{(n-j)} = (l_1^j l_2^{(n-j)})^\alpha , \quad (4.14)$$

which yields

$$\alpha = \frac{\ln p_1+(n/j-1)\ln p_2}{\ln l_1+(n/j-1)\ln l_2} . \quad (4.15)$$

In Fig. 7(c), we display the $f(\alpha)$ spectrum obtained from Eqs. (4.13) and (4.15). This spectrum is characteristic of a multifractal measure. The scaling exponent α takes on a value in a finite range: $\alpha_{\min} \leq \alpha \leq \alpha_{\max}$, where

$$\alpha_{\min} = D_{+\infty} = \ln p_2/\ln l_2 = 1, \quad f(\alpha_{\min}) = 0 \quad (4.16)$$

is associated with the symbolic sequence $LLL \cdots LLL \cdots$, which addresses the central point and corresponds to the region of highest mass; conversely,

$$\alpha_{\max} = D_{-\infty} = \ln p_1/\ln l_1 = \tfrac{3}{2}, \quad f(\alpha_{\max}) = 1 \quad (4.17)$$

is associated with the symbolic sequences S_{i_1}, S_{i_2}, $S_{i_3}, \ldots, S_{i_j}, S_{i_k}, \ldots$ (where $i = 1, \ldots, 4$ labels the selected small piece among the $m_1 = 4$ possible ones at each stage of the construction) that correspond to the regions of lowest mass: from Eq. (4.13) these regions have a finite density exponent $f(\alpha_{\max}) = 1$. Let us remark that the maximum of the $f(\alpha)$ curve gives the fractal dimension D_0 [Eq. (4.7) for $q = 0$]:

$$D_0 = 3 - \ln(\sqrt{17}-1)/\ln 2 \sim 1.357 . \quad (4.18)$$

In Fig. 7(a) we illustrate the numerical determination of D_q for $q \geq 0$, from slopes of graphs of $\ln Z_q/(q-1)$ versus $\ln\epsilon$ using the box-counting algorithm described in Sec. II B 1. As compared to the corresponding graphs obtained for the one-scale snowflake fractal [Fig. 3(a)], the graphs in Fig. 7(a) are well approximated by a straight line whose slope is no longer independent of q but ranges from $\alpha \sim \alpha_{\min} = 1$ for large values of q to $\alpha \sim 1.39$ for $q = 0$. At this point let us mention that we have also performed the fixed-mass computation of the D_q's for $q \leq 0$, together with the direct measurement of the $f(\alpha)$ spectrum using Eqs. (2.10) and (2.12). These results were found to be in good agreement with the

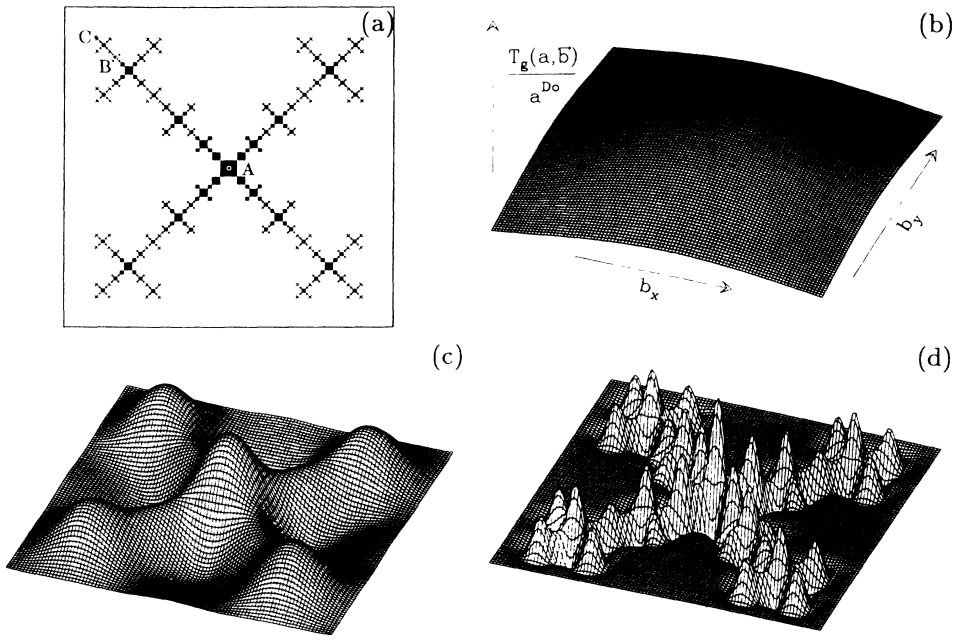

FIG. 8. Wavelet transforms of the two-scale snowflake fractal shown in (a). The analyzing wavelet is the radial Mexican hat defined in Eq. (3.23). The scale parameter a is successively divided by the same factor $l_1^{-1}=4$: (b) $a=a^*$, (c) $a^*/4$ and (d) $a^*/4^2$. $T_g(a,\mathbf{b})$ is expressed in a^{D_0} units in order to reveal the multifractality of the two-scale snowflake fractal ($D_0=1.357$).

theoretical predictions shown in Figs. 7(b) and 7(c), provided we initially proceeded through a rather large number of steps in the construction of the two-scale snowflake fractal. As previously pointed out, accurate dimension measurements require averaging over several periods of oscillation in the usual log-log procedure.

2. *Wavelet transforms*

In Figs. 8 and 9, we present the two-scale snowflake fractal shown in Fig. 8(a) as seen through the wavelet microscope when increasing the magnification factor a^{-1}. A three-dimensional representation is used in Fig. 7, while $T_g(a,\mathbf{b})$ is coded using 32 shades from white [$T_g(a,\mathbf{b})\leq 0$] to black [$\max T_g(a,\mathbf{b})>0$] in Fig. 9. In order to compare this analysis with the wavelet transform of the one-scale snowflake fractal (Sec. IV A 2) (and thus to test the ability of the wavelet transform to distinguish a multifractal from a globally self-similar aggregate), we actually show in Fig. 8, the spatial dependence of $\Upsilon_g(a,\mathbf{b})=a^{-D_0}T_g(a,\mathbf{b})$ where D_0 [Eq. (4.18)] is supposed to be known from previous box-counting or fixed-mass measurements. At large scales, $a\sim a^*$, the two-scale snowflake fractal looks like a single object [Figs. 8(b) and 9(a)]. When progressively decreasing the scale parameter a, the size of this object reduces to a characteristic size $a\sim l_2=\frac{1}{2}$, while four satellites emerge at each corner of this object [Fig. 9(b)]. These satellites have fully developed (with respect to the main peak) when one reaches the value $a=l_1=\frac{1}{4}$ [Fig. 8(c) and 9(c)]. As seen in the three-dimensional representation in Fig. 8(c), the wavelet transform of the two-scale snowflake fractal presents a mountainous landscape with a main peak of size $l_2=\frac{1}{2}$ at the center ($LLL\ldots LL\ldots$) and four identical hills of lowest height and size $l_1=\frac{1}{4}$ located at the points corresponding to the symbolic sequences $SLL\ldots LL\ldots$. Then when further increasing the magnification, the same process is repeated for (i) the main central peak which splits into a sharper central peak of size $l_2^2=\frac{1}{4}$ ($LLL\ldots LL\ldots$) [Fig. 9(d)] and four smaller peaks of size $l_2l_1=\frac{1}{8}$ ($LSL\ldots LL\ldots$), and (ii) the four satellites from which emerge four secondary peaks of size $l_1l_2=\frac{1}{8}$ ($SLL\ldots LL\ldots$) and 16 smaller peaks of size $l_1^2=\frac{1}{16}$ ($SSLL\ldots LL\ldots$) [Figs. 8(d) and 9(e)]. The snowflake in Fig. 8(a) is then obtained in the limit $a\rightarrow 0$, by subsequently applying the same rule [Fig. 9(f)]. The peaks that successively show up when increasing the magnification correspond to symbolic sequences with k symbols L and S and an infinite "tail" of L's. The peaks that have the same size and same height are addressed by symbolic sequences which possess the same number of L's and S's, respectively, in the k first symbols preceding the infinite tail of L's. Then, when further increasing the magnification, these peaks keep growing (they correspond to singularities of strength $\alpha<D_0$) in the three-dimensional representation shown in Fig. 8, while the height difference between peaks of different generations (i.e., associated with singularities of different strength) remains unchanged because of the infinite tail of L's in their symbolic sequence address. The mountainous landscapes shown in Fig. 8, with peaks of different heights corresponding to the strongest singularities, are thus typical of wavelet transforms of multifractal aggre-

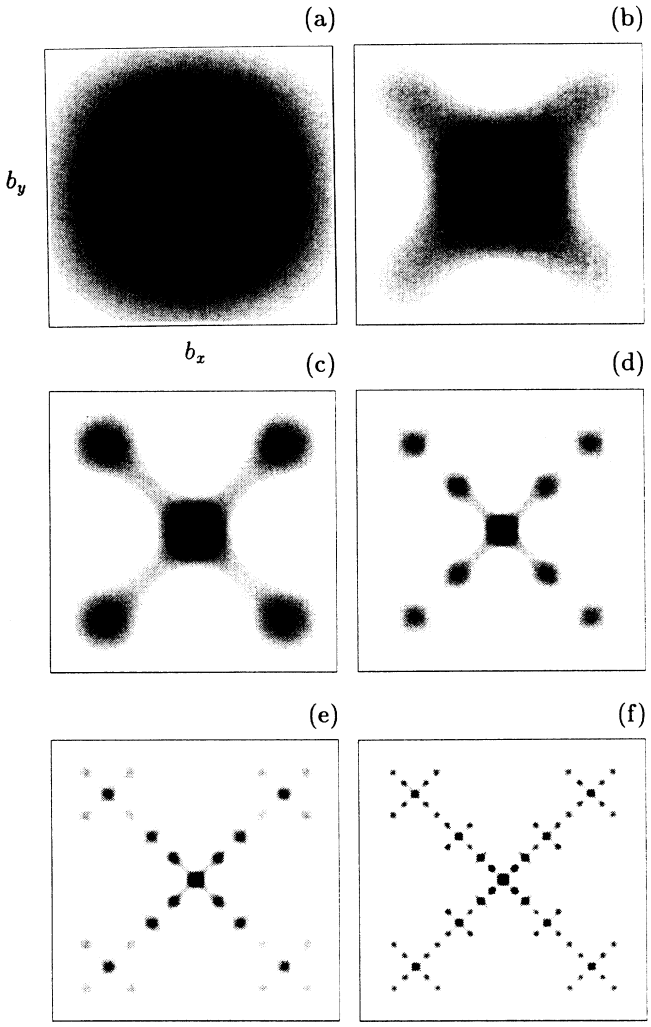

FIG. 9. Wavelet transforms of the two-scale snowflake fractal shown in Fig. 8(a). $T_g(a,\mathbf{b})$ is coded using 32 shades from white ($T_g \leq 0$) to black ($\max T_g > 0$) for each value of the scale parameter (a) $a = a^*$, (b) $a^*/2$ (c) $a^*/2^2$, (d) $a^*/2^3$, (e) $a^*/2^4$, and (f) $a^*/2^5$. The analyzing wavelet is defined in Eq. (3.23).

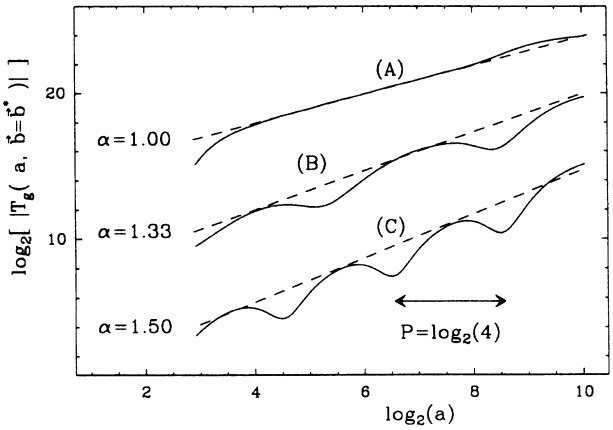

FIG. 10. Wavelet transforms of the two-scale snowflake fractal shown in Fig. 8(a). $\log_2|T_g(a,\mathbf{b}=\mathbf{b}^*)|$ vs $\log_2 a$ (arbitrary scales). The three curves correspond to the central point A(*LLL . . . LL . . .*) associated with the strongest singularity $\alpha=\alpha_{\min}=1$, the point C (*SSS . . . SS . . .*) associated with the weakest singularity $\alpha=\alpha_{\max}=\frac{3}{2}$ and the point B (*LSLS . . . LS . . .*) where $\alpha \simeq 1.33$. The analyzing wavelet is defined in Eq. (3.23).

gates. They drastically contrast with the landscapes in Fig. 4, where all the peaks have the same height as a direct consequence of the global self-similarity of the one-scale snowflake pattern.

Besides its ability to reveal the construction rules of a multiscale snowflake fractal (Figs. 8 and 9), the wavelet transform provides a very efficient tool to measure quantitatively the local scaling exponent $\alpha(\mathbf{x})$. At each point on the aggregate, $T_g(a,\mathbf{b})$ displays a power-law behavior; the exponent $\alpha(\mathbf{b})$ is found to vary from one point to the other, as shown in Fig. 10, where $T_g(a,\mathbf{b})$ is plotted versus a in a log-log scale representation. Disregarding finite-size effects at large scales and the ultraviolet cutoff (lattice mesh size) at small scales, the wavelet transform yields an accurate estimate of $\alpha(\mathbf{x})$, in good agreement with the theoretical predictions [Eq. (4.15)]. When one focuses $T_g(a,\mathbf{b}=\mathbf{b}_A)$ at the central point $\mathbf{b}_A$ (*LLL . . . LL . . .*), one extracts the slope $\alpha(\mathbf{b}_A)=\alpha_{\min}=1.0$, which is the predicted strength for the strongest singularity [Eq. (4.16)]. From the slope obtained at one ($\mathbf{b}_C$) among the 4^n points with symbolic sequence address *SSS . . . SS . . .*, one gets a remarkable estimate of $\alpha(\mathbf{b}_C)=\alpha_{\max}=1.50$ for the strength of the weakest singularities [Eq. (4.17)]. When one repeats this measurement for other less trivial symbolic sequences, e.g., $\mathbf{b}_B$ (*LSLSLS . . .*), one obtains values of α [$\alpha(\mathbf{b}_B)\simeq 1.33$] between these two extremes, which fit remarkably the theoretical values given by Eq. (4.15). To conclude, let us remark that $T_g(a,\mathbf{b})$ actually displays an oscillatory power-law behavior in the limit $a \to 0$ with two characteristic periods: $P_1=\ln l_1^{-1}=\ln 4$ and $P_2=\ln l_2^{-1}=\ln 2$. The oscillations with period P_1 have a large amplitude, as seen in Fig. 10 (point *C*). The oscillations with period P_2 have a rather small amplitude and are unnoticed (points *A* and *B*). Thus, the measurement of these periods provide a direct estimate of the two scale factors l_1 and l_2. Then with the additional information extracted from the exponent measurement $\alpha_{\min}=\ln p_2/\ln l_2$ at point *A* and $\alpha_{\max}=\ln p_1/\ln l_1$ at point *C*, one can deduce[40,41,61] the value of the measures p_1 and p_2 which leads to a complete knowledge of the structural complexity of the two-scale snowflake fractal shown in Fig. 8(a).

V. WAVELET TRANSFORM OF DIFFUSION-LIMITED AGGREGATES

A. Generalized fractal dimensions and $f(\alpha)$ spectrum

The DLA model introduced by Witten and Sander[6] can be regarded as describing cluster growth in the

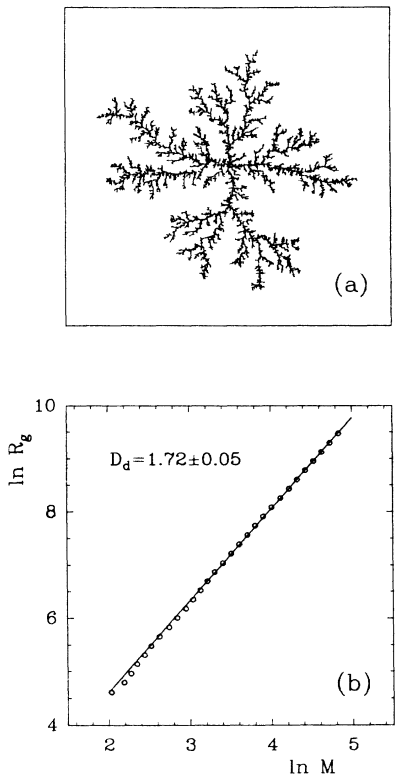

FIG. 11. (a) A DLA cluster of mass $M=13\times10^3$ computed on a square lattice with the original model of Witten and Sander (Ref. 6). (b) Dependence of the radius of gyration R_g on the cluster mass M; R_g is an average value over 50 independent DLA growths.

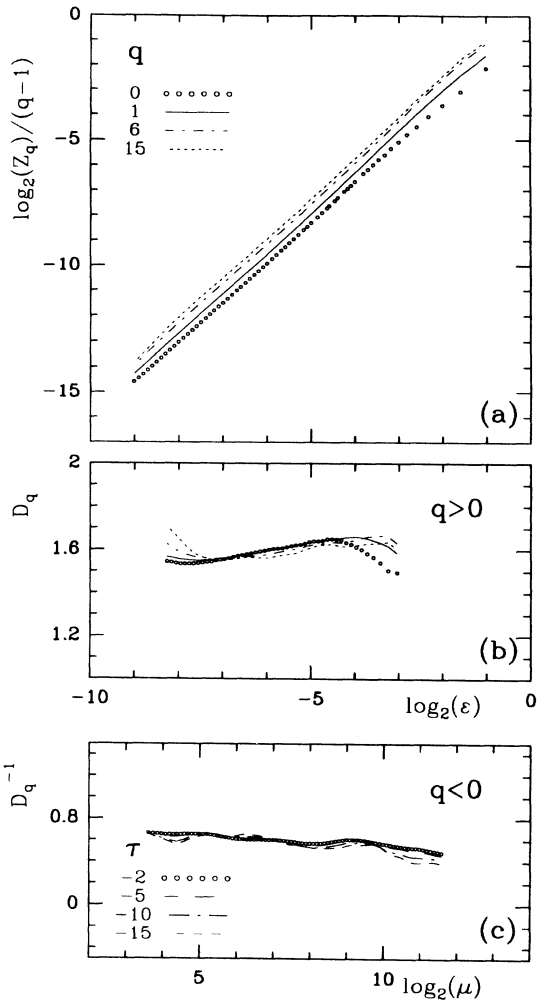

FIG. 12. These graphs illustrate the determination of the generalized fractal dimensions D_q for the DLA cluster shown in Fig. 11(a). (a) Box-counting computation of D_q for $q\geq0$. (b) The local dimensions D_q, given by the local slopes of the curves in (a) obtained from linear regression fits for the range $\Delta\log_2\epsilon=1$. (c) The local dimensions D_q^{-1} for $q<0$, obtained from local linear regression fits using fixed-mass computation ($\Delta\log_2\mu=1$).

diffusion field, because particles sticking to the cluster come far away through pure random walk. Although the tortuous shape of DLA clusters [Fig. 11(a)] makes them seem quite different from regular snowflakes [Fig. 4(a)], recent numerical studies have pointed out some morphological change of the overall profile of DLA patterns to more or less regular shapes when some anisotropy is introduced either in the sticking rule or in the random walk.[15,23-29] But such an anisotropy can also be induced by the underlying lattice in the limit of large mass clusters (Refs. 8, 14–16, 23–25, 27, 28 and 117–119). This anisotropy can even show up for small clusters when using a noise-reduced version of the DLA model.[27] In their original paper, Witten and Sander[6] found that the dynamical dimension D_d describing the dependence of the weight of a cluster (number of occupied site) on its average radius of gyration *during the growth process* was $D_d=1.70\pm0.02$, while the dimension D_2 extracted from the density-density correlation function of the cluster *at the end of the growth* was smaller, $D_2=1.66\pm0.01$. Subsequent numerical simulations[11-14,120] have corroborated the result that D_d is larger than D_2 and D_0 as issued from box-counting measurements.

Here we compute not only the fractal dimension D_0 and the correlation dimension D_2 (as in previous works), but also the whole spectrum of generalized fractal dimensions D_q, and we find that within the uncertainties the D_q are the same. The DLA cluster shown in Fig. 11(a) was computed using the on-square lattice algorithm proposed by Ball and Brady.[14] In order to avoid anisotropic growth induced by the underlying lattice, we focus our attention on clusters of small mass ($M\leq15\times10^3$ particles); these clusters are expected to be of the same nature as those computed using off-lattice algorithms where disks of elementary size diffuse in a continuous medium.[121] As previously mentioned in Sec. II B, the boundary of the DLA clusters is taken to be given not by a discrete set of points but by elementary square cells centered at each border point.[91] The box-counting analysis for $q\geq0$ is shown in Figs. 12(a) and 12(b); this analysis

yields $D_q = 1.60 \pm 0.02$, independent of q for an ϵ range of nearly two decades. Moreover, the values of D_q for $q < 0$, as obtained with the fixed-mass algorithm [Fig. 12(c)], are in excellent agreement with the D_q values for $q \geq 0$. We have conducted a similar analysis for DLA clusters grown on a triangular lattice which confirms that our numerical estimate of D_q is not affected by the anisotropy of the underlying lattice. Similar analysis for clusters of 3000–50 000 particles have not revealed any significant change in the measured value of D_q. These observations strengthen the results of previous simulations[91] performed in a strip geometry with periodic boundary conditions and converge to the conclusion that small mass on-lattice DLA clusters are statistically self-similar with dimensions

$$D_q = 1.60 \pm 0.02 , \tag{5.1}$$

independent of q. The corresponding $f(\alpha)$ spectrum is thus concentrated on a single point:

$$\alpha = 1.60, \quad f(\alpha = 1.60) = 1.60 . \tag{5.2}$$

At this point, let us note that our estimate of D_q [Eq. (5.1)], as well as previous box-counting[12,72] and point-wise[15] computations of the fractal dimension D_0, is significantly smaller than numerical estimates[6,12–15] and theoretical predictions[7–10] for the dynamical dimension $D_d (\sim 1.71)$ deduced from the evolution of the radius of gyration during cluster growth. This observation is confirmed in Fig. 11 where the dynamical dimension computed during the growth of 50 on-lattice DLA clusters is found to be unambiguously larger than D_0: $D_d = 1.72 \pm 0.05$. The possible reason for this discrepancy between D_d and D_0 is that, in computing the depen-

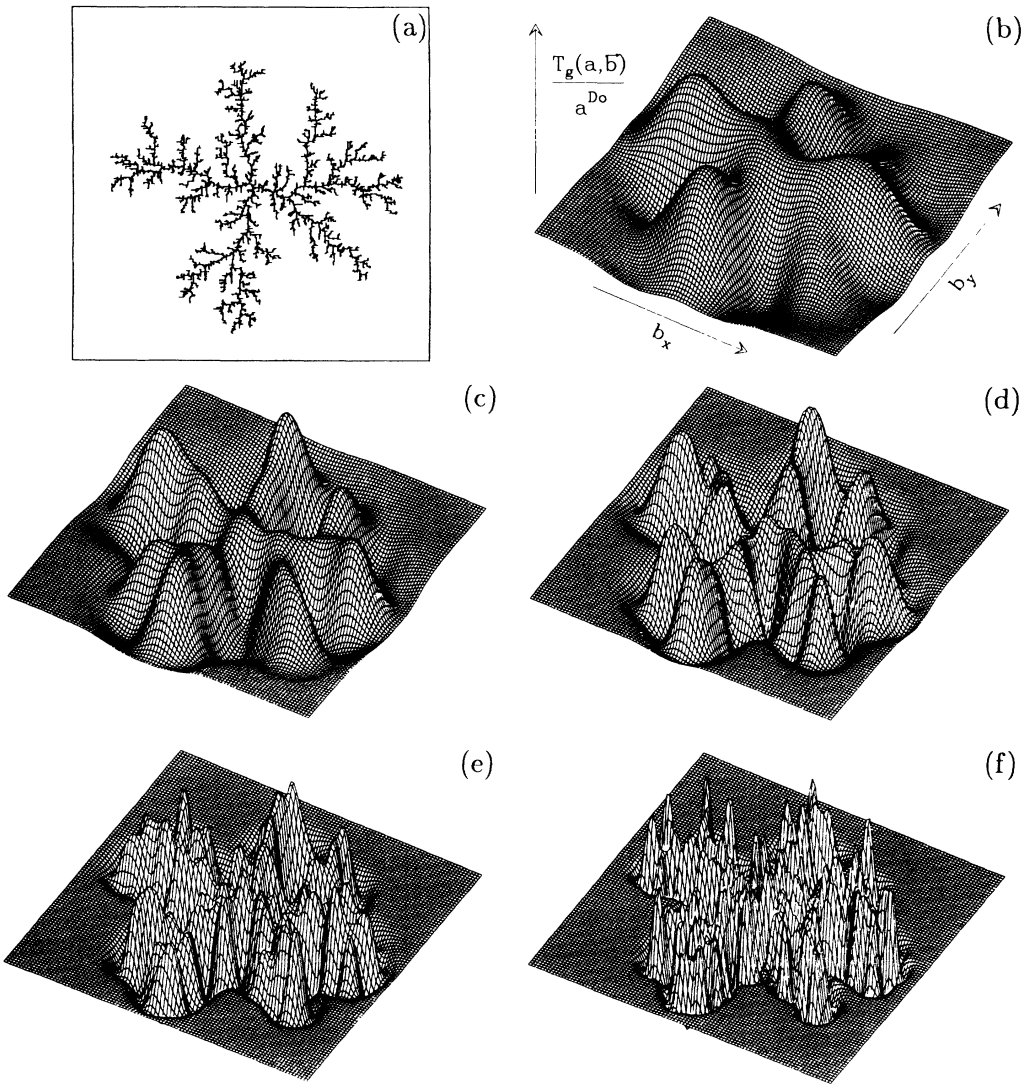

FIG. 13. Wavelet transforms of the ($M = 5465$ particles) DLA cluster shown in (a). The analyzing wavelet is the radial Mexican hat defined in Eq. (3.23). The scale parameter a is successively divided by the same factor $\delta = 1.55$; (b) $a = a^*$, (c) a^*/δ, (d) a^*/δ^2, (e) a^*/δ^3, and (f) a^*/δ^4. $T_g(a,\mathbf{b})$ is expressed in $a^{1.60}$ units in order to reveal the global self-similarity of the geometry of DLA clusters (singularities of unique strength $\alpha \sim 1.60$).

dence of the radius of gyration R as a function of the mass of the growing cluster, one underestimates the number of occupied sites that will actually be contained in a disk (centered on the original seed) of radius R at the end of the growth. Since this undershoot seems to be less and less dramatic when increasing the mass of the cluster, it is very likely that asymptotically D_d and D_0 converge to a unique value. So far there has been no definite numerical proof of this conjecture. Let us mention that in a recent study,[16] D_d has been found to decrease during the early stages of growth. The use of D_d instead of D_0 is probably the reason that a previous study[30] failed to reveal the self-similar structure of DLA clusters.

B. Wavelet transforms

Figure 13 shows the wavelet transform[74] of a DLA cluster of mass $M=5645$ through different panels corresponding to decreasing values of the scale parameter a. To best reveal the global self-similarity of this aggregate, these panels actually illustrate the spatial dependence of $\Upsilon_g(a,\mathbf{b})=a^{-1.60}T_g(a,\mathbf{b})$. As already experienced in our previous analysis of snowflake fractals in Sec. IV, the wavelet microscope provides insight into thinner and thinner internal details in the shape of DLA patterns. But what is remarkable in Figs. 13(b)–13(f) is that everywhere in the plane, the DLA pattern branches at the same rate when the magnification factor is increased: $\Upsilon_g(a,\mathbf{b})$ does not display any significant dependence upon the translation parameter $\mathbf{b}$ provided the wavelet transform points to a cluster particle. The laser prints in Fig. 14, where $T_g(a,\mathbf{b})$ is coded using 32 shades from white [$T_g(a,\mathbf{b})\leq 0$] to black [$\max T_g(a,\mathbf{b})>0$], are very suggestive of the fact that, as seen through the wavelet microscope, DLA clusters look very much like viscous fingers.[1–5,19,120] When a is decreased, the main fingers observed at large scales [Figs. 14(a) and 14(b)], split into fingers of smaller width, among which one can distinguish secondary fingers which appear on the side of the main fingers [Figs. 14(c) and 14(d)]. This structuration of the cluster boundary when the magnification parameter a^{-1} is increased presents a strong analogy with the tip-splitting and side branching instabilities observed dynamically in viscous finger experiments.[122–126] In the limit $a\to 0$ [Figs. 14(e) and 14(f)], the width of the fingers keeps decreasing until it reaches the particle size (which is very likely to play the role of the capillary length in viscous fingering), while successive generations of fingers are brought to light. Then one recovers the DLA pattern with its arborescent structure.

As sketched in Figs. 14(c) and 14(f), the self-similarity of DLA patterns is strongly related to the existence of a characteristic screening angle β between branches of two successive generations.[1–5,127] Even though our statistical sample is not large enough to allow us to produce any reliable estimate of this angle, our average value is quite compatible with a rough pentagonal symmetry $\langle\beta\rangle\sim 36°$. The presence of a fivefold symmetry in diffusion-limited aggregation has already been suggested in previous works.[7–9,128] In a related study of a random fractal automaton[129] it has been shown that the rotational symmetry is actually broken at a screening angle of about $4\pi/5$, where DLA-like patterns occur. This critical angle also shows up in the shadowing effects which are inherent to fractal growth processes.[130] We refer the reader to a recent comparative study[131] of unstable viscous fingers and DLA clusters grown in different geometries (linear channel, radial configuration, and sector-shaped cells) which underlines the fivefold symmetry in both these growth mechanisms and brings more convincing indications that one can pursue to a quantitative level the analogy between diffusion-limited aggregation and viscous fingering in isotropic Newtonian fluids.

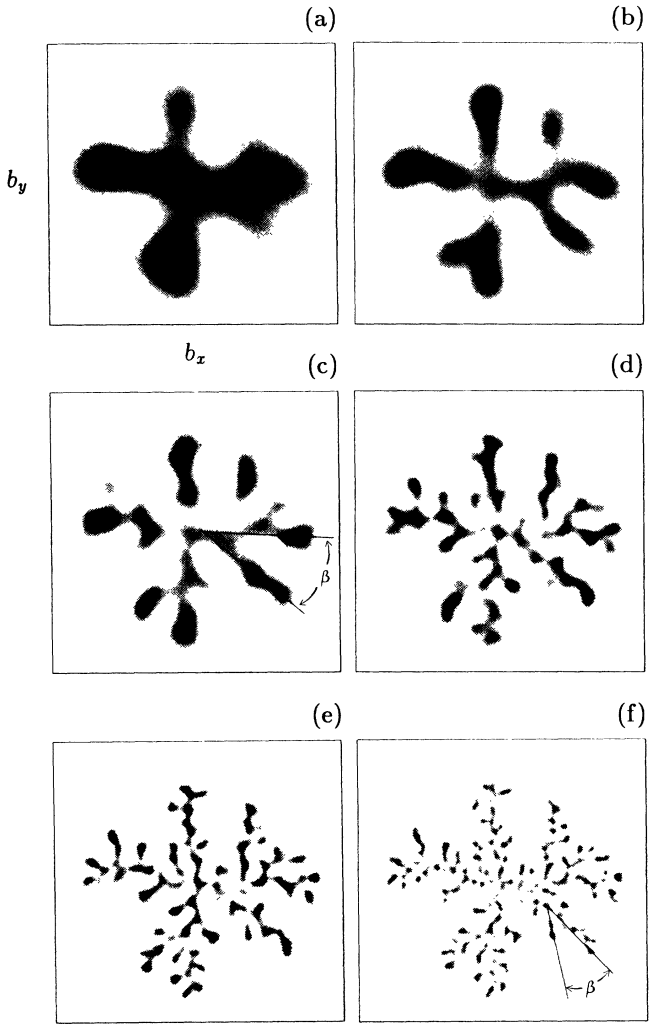

FIG. 14. Wavelet transforms of the ($M=5465$ particles) DLA cluster shown in Fig. 13(a). $T_g(a,\mathbf{b})$ is coded using 32 shades from white ($T_g\leq 0$) to black ($\max T_g>0$) for each value of the scale parameter (a) $a=a^*$, (b) a^*/δ, (c) a^*/δ^2, (d) a^*/δ^3, (e) a^*/δ^4, and (f) a^*/δ^5 where $\delta=1.55$. An average angle $\langle\beta\rangle$ can be defined over a wide range of scales as characterizing screening effects in DLA growth process. The analyzing wavelet is defined in Eq. (3.23).

In Fig. 15, $T_g(a,\mathbf{b})$ is plotted versus a in a log-log scale

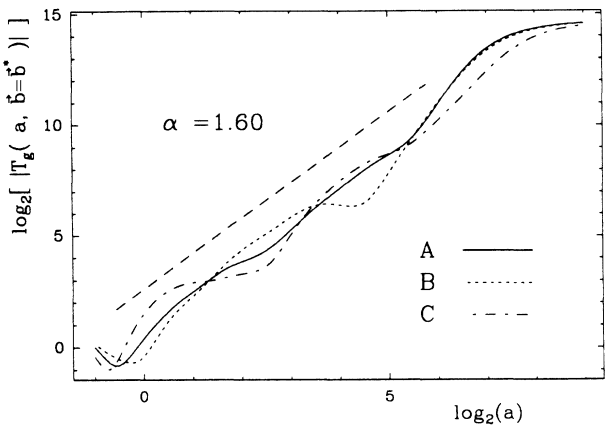

FIG. 15. Wavelet transforms of the DLA cluster of mass $M = 13 \times 10^3$ particles shown in Fig. 11(a). $\log_2|T_g(a,\mathbf{b}=\mathbf{b}^*)|$ vs $\log_2 a$ (arbitrary scales). The three curves correspond to the central seed A ($\mathbf{b}^* = \mathbf{b}_A$) (solid line) and to two other points B ($\mathbf{b}^* = \mathbf{b}_B$) (dashed line) and C ($\mathbf{b}^* = \mathbf{b}_C$) (dashed-dotted line) arbitrarily chosen on the cluster boundary. The analyzing wavelet is defined in Eq. (3.23).

representation. The measurement of the local scaling index $\alpha(\mathbf{b})$ is affected (i) at large scales by finite-size effects (the fact that M is finite also enhances the privileged role played by the seed particle at the center of the cluster);[132,133] and (ii) at small scales by the ultraviolet cutoff induced by the mesh of the underlying lattice (sticking length). Taking care of these experimental difficulties, we have carried out a rather systematic (log-log) investigation of the a dependence of $T_g(a,\mathbf{b})$ all over the DLA cluster shown in Fig. 11(a). We have reproduced this analysis for different DLA clusters with mass $M \leq 15 \times 10^3$. As previously suspected from the qualitative survey in Fig. 13, the collected data bring definite evidence for the global self-similarity of DLA clusters with a unique local scaling exponent $\alpha \sim 1.60$. This observation demonstrates that the $f(\alpha)$ spectrum reduces to a single point $f(\alpha = 1.60) = 1.60$ [Eq. (5.2)] and consequently that the generalized fractal dimensions coincide $D_q = 1.60$, $\forall q$ [Eq. (5.1)].

However, beyond the local character of the wavelet transform analysis, the actual self-similarity of DLA patterns still remains at a statistical level. As shown in Fig. 15, $T_g(a,\mathbf{b})$ displays an oscillatory power-law decrease in the limit $a \to 0$. But in contrast to the wavelet transforms of self-similar snowflake fractals (Fig. 6), the oscillations around the straight line in the log-log procedure are apparently not periodic. This observation raises several questions of fundamental importance. First one can wonder whether this aperiodicity persists at smaller scales in the limit of large mass DLA clusters. Then if one is able to confirm numerically the existence of aperiodicity, one must decide whether this departure from periodicity is external noise or deterministic chaos.[134–137] Noisy oscillations would mean that DLA clusters are random fractals that are generated by a nondeterministic construction rule.[23,69] Conversely, chaotic oscillations would rather indicate that DLA clusters are chaotic fractals that are constructed according to a deterministic recursive process.[70–72] Unfortunately, the range of accessible length scales for small mass on-lattice clusters is only a few fundamental periods of oscillation wide and much larger off-lattice clusters are needed to answer unambiguously this interrogation. However, on the basis of the observation that the numerical aperiodicity concerns a range of length scales which is much larger than the step size s (the fundamental period of oscillation in Fig. 15 is about four units in $\log_2$ scale), it is quite out of the question that the complexity of DLA patterns result from the random arrival positions of the discrete accreting particles. External noise only affects the small-scale behavior of the wavelet transform ($a \sim s$) and thus cannot be responsible for chaotic behavior observed at larger scales.

The results of our wavelet transform analysis of DLA patterns are thus much more on the line of the deterministic approach developed by Sander and collaborators.[70–72] The branched geometry of DLA clusters is very likely to be the expression of a nonlinear chaotic recursive construction process, which accounts for the proliferation of tip-splitting and side-branching instabilities observed during the growth. In particular, the sequences of screening angles $\beta_1, \beta_2, \ldots, \beta_n, \ldots$ between branches of successive generations are apparently chaotic sequences. There exist spatial correlations between branches; for example, when the screening angle β_n is small at a given stage, then the screening angle β_{n+1} at the next stage is very likely to be large. In a forthcoming publication we plan to investigate the deterministic nature of these sequences which are at the heart of the construction rules of DLA fractal patterns. As far as the deterministic issue is concerned, we will specially analyze the oscillating power-law behavior of the wavelet transforms of large mass off-lattice DLA clusters, using numerical techniques inspired from dynamical systems theory,[134–137] e.g., phase portrait reconstruction, Poincaré sections, one-dimensional (1D) maps, etc. Our hope is to extract a well-defined 1D map from the wavelet transform data that will bring the first unambiguous proof that DLA patterns result from a cascade of spatiotemporal bifurcations.

VI. WAVELET TRANSFORM OF ELECTRODEPOSITION CLUSTERS

Electrodeposition of metals from electrolytes offers a very attractive way to study pattern forming phenomena.[84] Various experiments with a variety of metals have revealed dramatic changes in the morphology of the deposits according to the precise conditions of deposition. Essentially three regimes of growth have been identified in two-dimensional electrodeposition experiments: (i) dense radial patterns[85] which tipsplit repeatedly with a very small screening angle and thus fill space and have a stable overall outline, (ii) dendritic crystal patterns[86,87] which have an ordered structure with stable tips and side branches (these dendritic clusters resemble snowflakes and result from a directional growth mechanism); and (iii) disordered fractal patterns[86,88–91] with no evidence of

preferred direction of growth and which strongly resemble the clusters produced by the diffusion-limited aggregation model of Witten and Sander.[6] Most of the metals examined thus far have produced these three major categories of morphology, with one exception, copper, for which the formation of dendritic clusters is apparently inhibited.[84]

DLA-like fractal morphology has been the subject of various experimental studies[88–91] with mainly zinc and copper metals. Different configurations have been considered, e.g., radial geometry[85–89] or strip geometry.[90,91] But thus far, most experiments[85–91] have been conducted when varying independently the concentration of metal ions and the cathode potential. As theoretically expected,[84] DLA-like patterns have been identified at small voltage and small concentration when the diffusion length becomes large as compared to the size of the deposit itself, i.e., when the growth is slow. In pioneering experimental studies,[86,88–90] the disordered structure of the electrodeposition clusters was quantitatively compared to the fractal geometry of DLA patterns through the numerical computation of the fractal dimension D_0 only. This dimension was found to vary from 1.66 ± 0.03 (Ref. 89) to 1.75 ± 0.03 (Ref. 87), in rather good agreement agreement with the well-admitted value of the dynamical dimension $D_d \sim 1.70$ for DLA clusters.[6,17]

In a previous work,[91] in collaboration with Swinney, we did revisit these analyses of the fractal morphology of electrochemical deposits using box-counting and fixed-mass computations of the whole spectrum of generalized fractal dimensions D_q. The experimental configuration was zinc electrodeposition in a thin layer between two rectangular plates. The zinc electrodeposition clusters in the limit of small ionic concentration and small voltage were found globally self-similar with $D_q = 1.66\pm0.08$, independently of q. The analogy with the DLA growth process was strengthened by a comparative analysis of small-mass clusters grown in a strip geometry which brought evidence for the global self-similarity of DLA clusters, with $D_q = 1.60\pm0.02$. In this section, we use the wavelet transform to make a more accurate the quantitative comparison between the electrodeposition mechanism and diffusion-limited aggregation. For the sake of generality, we consider a configuration which differs substantially from our earlier experiment: two-dimensional copper electrodeposition clusters are grown in a circular geometry by applying a fixed current through the cell instead of a fixed potential difference. This is because for steady-state current flow, we know that the equations describing the growth are of an identical form as in the diffusion-limited case.[84] Consequently this configuration should permit a more reliable quantitative analysis of DLA like fractal growth in electrodeposition experiments.

A. Experimental details

The experimental configuration is a thin layer of a $0.05M$ $CuSO_4$ solution confined between two glass plates. The gap between the plates is 0.1 mm. A circular copper electrode of diameter 10 cm surrounds the fluid, and a copper cathode of diameter 0.1 mm is introduced vertically through a hole in the upper plate centered within the ring. The electrodeposition is initiated by applying a constant current $I = 0.1$ mA between the anode and the cathode. Then copper trees grow two-dimensionally from the tip of the cathode toward the outside for about 45–50 min without any abrupt change in the intricately branched geometrical structure of the clusters. At a late stage of growth these trees have grown to the size of a few centimeters. The system is illuminated with white light from below and photographed (at intervals of 30 s) from above with a 35-mm camera with magnification from 1 to 10×. Photographs of the cluster are digitized (512×512) and intensity levels above a threshold are taken to define the boundary of a cluster. The size of each pixel is enough for the resolution of the thickness of the branches. The cluster boundaries are quite sharp, and the results of our dimension computations (Sec. VI B) and wavelet transform analysis (Sec. VI C) are rather insensitive to the arbitrarily chosen threshold. The experimental apparatus is shown in Fig. 16.

B. Generalized fractal dimensions and $f(\alpha)$ spectrum

In the imaging data memory of the computer, the boundary of the electrodeposition clusters is defined by elementary cells centered at each boundary pixel, and the values of μ_i in the fixed-size partition function [Eq. (2.1)] are calculated from the portion of area of these cells in each box of the box-counting grid.[91]

The box-counting determination of D_q for $q \geq 0$ is shown in Figs. 17(a) and 17(b). On a wide range of scales $2^{-9} < \epsilon < 2^{-4}$, the local dimensions D_q [the slopes of the graphs $\ln Z_q/(q-1)$ versus $\ln\epsilon$] depend very weakly on both ϵ and q. The results for different q are all approximated by $D_q = 1.63\pm0.03$. At larger scales finite-size effects become important and the slope increases before ultimately decreasing for $\epsilon \geq 2^{-3}$. In contrast with our previous analysis of Zn electrodeposits,[91] we do not observe any decrease of the local dimensions at small scales due to the finite thickness of the electrodeposit branches; the size of one pixel ($\epsilon = 2^{-9}$) is actually slightly smaller than the thickness of the branches.

For $q < 0$, the values of D_q are determined using fixed-mass computations. The estimation of the local dimensions obtained by averaging over 400 randomly chosen centers is illustrated in Fig. 17(c) for several values of

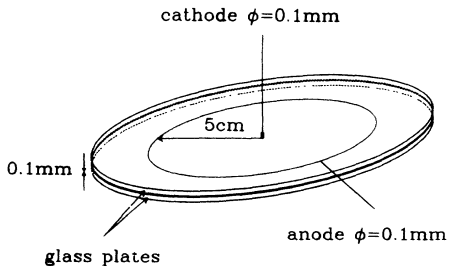

FIG. 16. Schematic of the electrochemical radial cell.

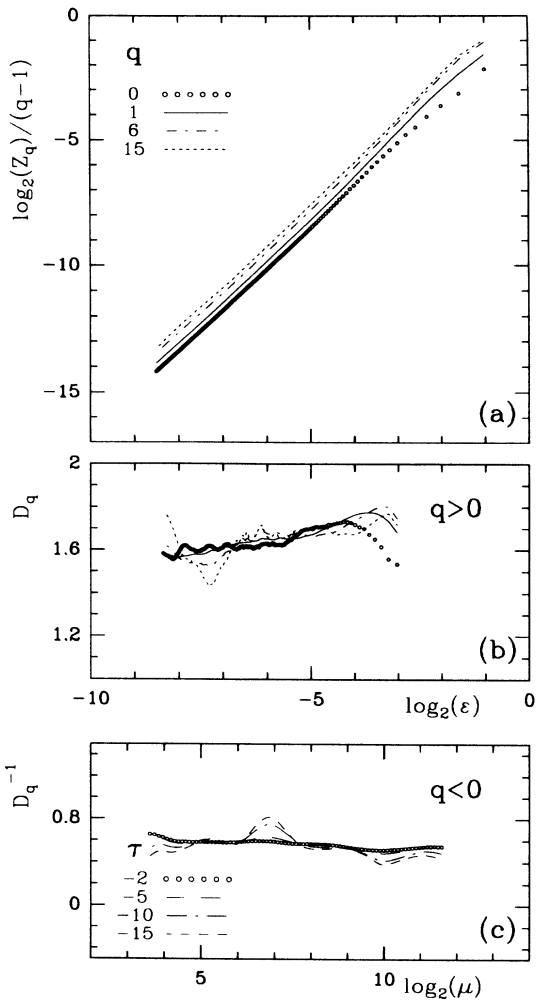

FIG. 17. These graphs illustrate the determination of the generalized fractal dimensions D_q for the copper electrodeposition cluster shown in Fig. 19(a). (a) Box-counting computation of D_q for $q \geq 0$. (b) The local dimensions D_q given by the local slopes of the curves in (a) obtained from linear regression fits for the range $\Delta \log_2 \epsilon = 1$. (c) The local dimensions D_q^{-1} for $q < 0$, obtained from local linear regression fits using fixed-mass computation ($\Delta \log_2 \mu = 1$).

$\tau < 0$ ($q = 1 + \tau/D_q$). The values of D_q for all q are consistent with the estimates obtained for $q \geq 0$, suggesting that the copper electrodeposition clusters observed at low ionic concentration and low current are statistically self-similar with dimensions

$$D_q = 1.63 \pm 0.03 , \tag{6.1}$$

independent of q. The scaling properties of these clusters are thus characterized by a $f(\alpha)$ spectrum of singularities which reduces to a single point

$$\alpha = 1.63, \; f(\alpha = 1.63) = 1.63 . \tag{6.2}$$

The remarkable quantitative agreement between Fig. 17 and 12 corroborates the conclusions of our previous experimental analysis of zinc electrodeposits[91] and strongly suggests that, at least at a statistical level, the geometry of electrodeposition clusters realizes the geometrical complexity of the theoretically proposed diffusion-limited aggregates.[6]

C. Wavelet transforms

Figures 18 and 19 show a survey of the wavelet transform analysis of the copper electrodeposition cluster presented in Fig. 19(a). To best reveal the global self-similarity of this aggregate, we proceed in a manner similar to DLA patterns in Fig. 13, i.e., we illustrate in Fig. 18 the spatial dependence of $\Upsilon_g(a,\mathbf{b}) = a^{-D_0} T_g(a,\mathbf{b})$ where $D_0 = 1.63$ according to our previous estimate in Eq. (6.1). When the magnification is increased, $\Upsilon_g(a,\mathbf{b})$ actually evolves from a hilly to a mountainous landscape with an increasing number of peaks of about the same height. As discussed in Sec. IV B, the fact that all over the cluster there is no hierarchy in the height of the proliferating peaks in $\Upsilon_g(a,\mathbf{b})$ shows a strong indication that the electrodeposition cluster in Fig. 13(a) is a globally self-similar fractal aggregate. This observation is made more quantitative in Fig. 20, where $T_g(a,\mathbf{b})$ is plotted versus the scale parameter a in a log-log scale representation. The measurement of the local scaling exponent $\alpha(\mathbf{b})$ is mainly affected at large scales by finite-size effects. With respect to the wavelet transform of DLA clusters there is no other bias at small scales than the ultraviolet cutoff induced by the imaging data analysis; as previously mentioned, the pixel size is slightly smaller than the thickness of the electrodeposit branches and at that resolution one does not observe any significant departure from bidimensionality in the growth process. Taking care that the central seed plays a privileged role because of the abnormally large size of the tip of the cathode, we have measured the exponent $\alpha(\mathbf{b})$ at different points selected at random on the copper electrodeposit in Fig. 19(a), discarding points lying too close to the cathode. The results shown in Fig. 20 for two arbitrarily chosen points are representative of the data we have collected; they bring a strong indication that the exponent $\alpha(\mathbf{b})$ does not depend on the position $\mathbf{b}$ on the cluster where the wavelet microscope is centered. Moreover, despite intrinsic oscillations around the straight line in the log-log plot in Fig. 20, this local exponent is found to be in remarkable agreement with the value $\alpha = 1.63$ [Eq. (6.2)] deduced from (global) box-counting and fixed-mass computations of the D_q's. These local measurements demonstrate that the $f(\alpha)$ spectrum reduces to a single point $f(\alpha = 1.63) = 1.63$, as expected for a globally self-similar aggregate. As far as the nature of the oscillations in the log-log representation of $T_g(a,\mathbf{b})$ is concerned, the accessible range of scales in Fig. 20 is not large enough to allow us to decide whether they are periodic or chaotic. However, let us point our that the (main) characteristic frequency of the oscillations obtained for copper electrodeposition clusters (Fig. 20) is strikingly similar to the characteristic frequency previously observed for DLA patterns (Fig. 15).

In Fig. 19, $T_g(a,\mathbf{b})$ is coded using 32 shades from white

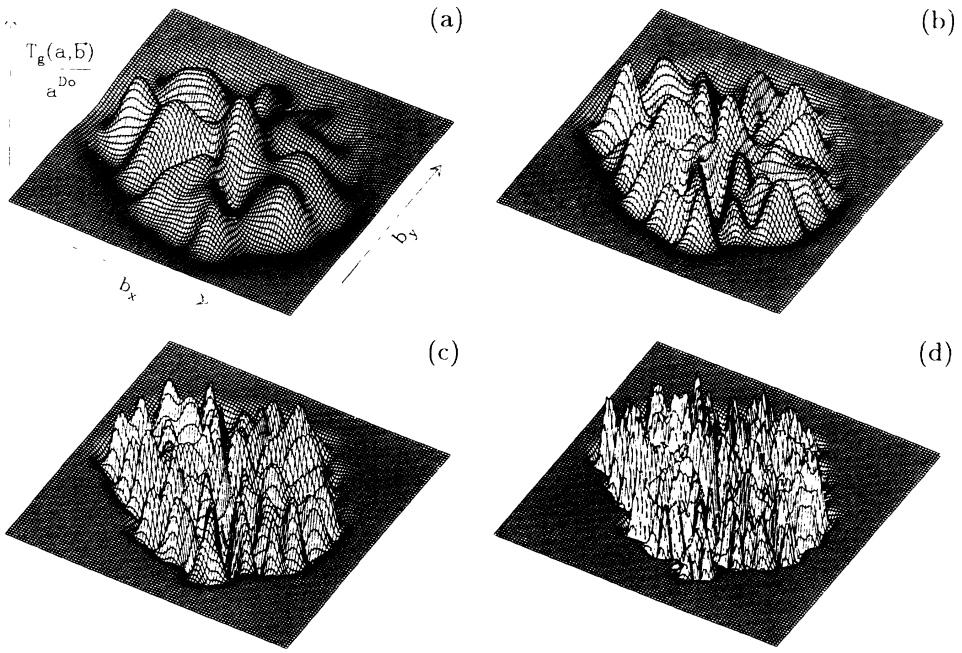

FIG. 18. Wavelet transforms of the copper electrodeposition cluster shown in Fig. 19(a). The analyzing wavelet is the radial Mexican hat defined in Eq. (3.23). The scale parameter a is successively divided by the same factor $\delta=1.55$: (a) $a=a^*$, (b) a^*/δ, (c) a^*/δ^2, and (d) a^*/δ^4. $T_g(a,\mathbf{b})$ is expressed in a^{D_0} units, $D_0=1.63$, in order to reveal the global self-similarity of the geometry of copper electrodeposition clusters (singularities of unique strength $\alpha\sim 1.63$).

$[T_g(a,\mathbf{b})\leq 0]$ to black $[\max T_g(a,\mathbf{b})>0]$. When decreasing the scale parameter a from large scales, one recovers macroscopic fingers [Figs. 19(b) and 19(c)] which break into smaller fingers [Figs. 19(d) and 19(e)] according to a scenario which reminds the tip-splitting and side-branching instabilities observed in viscous fingering experiments.[122–126] One feature that is remarkable in this scenario is the fact that at any scale, the self-similarity of the copper electrodeposition cluster involves a characteristic screening angle β between branches of two successive generations whose average value is quite compatible with the fivefold symmetry emphasized for DLA patterns in Sec. V (Fig. 14): $\langle\beta\rangle\sim 36°$. Very recently, Couder and collaborators[125] have reported similar observations in the investigation of unstable viscous fingers in a radial configuration. This underlying fivefold symmetry seems to be a key point in the understanding of fractal growth processes in a Laplacian field. Let us mention that when investigating the parameter space ($[CuSo_4]$,I), we have met conditions close to DLA growth where some locking in the electrodeposition mechanism yields a regular growth of five needle crystals equally spaced without any branching during the growth (~ 15 min).

To summarize, the wavelet transform analysis of the copper electrodeposition cluster shown in Fig. 19(a) brings definite evidence for the existence of a unique scaling exponent $\alpha=1.63\pm 0.03$. This exponent accounts for the local scaling properties over the entire aggregate. Its value is in remarkable agreement with the exponent $\alpha=1.60\pm 0.02$ found for DLA patterns in Sec. V. A quantitative understanding of this scaling exponent value in terms of the suspected fivefold symmetry would be a major step towards the development of a unified theory for growth processes which take place in a Laplacian field, the growth velocity of the patterns being proportional to the local gradient of this field. We hope to elaborate on this point in a forthcoming publication.

VII. CONCLUSION

Most previous characterizations of fractal aggregates arising in physics have relied upon a few "universal numbers" such as the Hausdorff and correlation dimensions.[1–5] Recently, the notion of dimensions has been generalized to the so-called generalized fractal dimensions D_q. These dimensions are closely related to the continuous spectrum of exponents α and their spectrum $f(\alpha)$. However, this spectrum only reflects the statistical contributions of each of these singularities but fails to memorize their spatial locations. In this paper, we have introduced a new mathematical technique: the wavelet transform, which is capable of characterizing the full geometrical complexity of these aggregates. In fact, this mathematical microscope is a natural tool for investigating the local scaling properties of these aggregates. When increasing the magnification factor, the wavelet microscope provides an insight into the inner structural hierarchy of the aggregates, revealing in a spectacular way, the construction rules of these objects, as shown in Sec. IV for snowflake fractals.

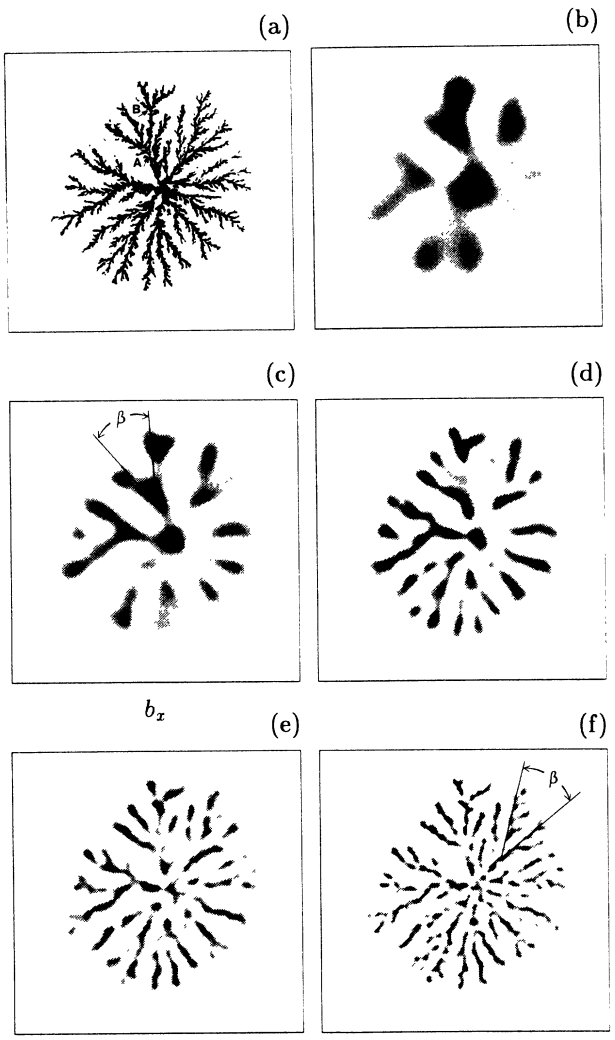

FIG. 19. Wavelet transforms of the copper electrodeposition cluster shown in (a). $T_g(a,\mathbf{b})$ is coded using 32 shades from white ($T_g \leq 0$) to black ($\max T_g > 0$) for each value of the scale parameter (b) $a = a^*$, (c) a^*/δ, (d) a^*/δ^2, (e) a^*/δ^3, and (f) a^*/δ^4 where $\delta = 1.55$. An average angle $\langle\beta\rangle \sim 36°$ can be defined over a wide range of scales as characterizing screening effects in electrodeposition process. The analyzing wavelet is defined in Eq. (3.23).

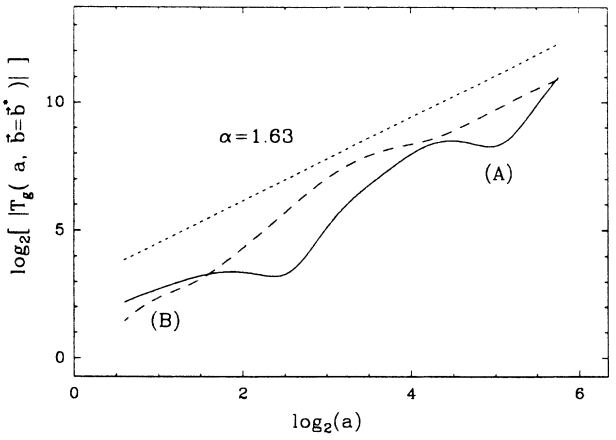

FIG. 20. Wavelet transforms of the copper electrodeposition cluster shown in Fig. 19(a). $\log_2|T_g(a,\mathbf{b})|$ vs $\log_2 a$ (arbitrary scales). The two curves correspond to points A ($\mathbf{b}^* = \mathbf{b}_A$) and B($\mathbf{b}^* = \mathbf{b}_B$) arbitrarily chosen on the cluster boundary [Fig. 19(a)]. The analyzing wavelet is defined in Eq. (3.23).

We have further applied the wavelet transform to numerical and experimental aggregates. The results reported in Sec. V and VI provide the first unambiguous evidence that two-dimensional clusters formed in DLA simulations and electrodeposition experiments (in the limit of low ionic concentration and low current) are globally self-similar fractals. The unique local scaling exponent $\alpha = 1.60$ for DLA clusters and $\alpha = 1.63$ for electrodeposition clusters are the same within experimental uncertainty. As seen through the wavelet microscope, diffusion-limited aggregates and electrodeposition clusters have a similar geometrical structure and are very likely to belong to the same universality class.

This conclusion seems to be (at least apparently) in contradiction with the results of previous studies[72,76–81] of the kinetic properties of growing DLA clusters. Numerical calculations have revealed that the growth process is actually not self-similar; in particular, the growth probability measure (perimeter occupancy probability) has a finite range of scaling indices, and the $f(\alpha)$ spectrum is a convex function similar to those found for multifractal measures. The sticking probability distribution is thus a nonhomogeneous distribution over the cluster perimeter; the physical basis for this fact is that the ("hot") tips of the main branches correspond to an active region of growth, while the growth of many "cold" tips and fjords is invisibly small if not totally aborted as the result of screening effects.[138] In a forthcoming publication[75] we will develop a wavelet transform analysis of the multifractal properties of the sticking probability measure. Our goal will be to elucidate this screening mechanism in order to make the connection between the multifractal character of the growth process and the global self-similarity of the geometry of the growing patterns. As pointed out in Sec. V, our expectations rely upon the potential capabilities of the wavelet transform to provide the foundations for a renormalization-group approach of growth processes which take place in a Laplacian field.[41] The wavelet transform analysis of the geometry of DLA patterns performed in Sec. V strongly suggests that the structural self-similarity of DLA clusters is very likely to be understood as averaging over the invariant measure of a deterministic iterative construction process which displays chaotic behavior. Along this line the scaling properties of diffusion-limited aggregates would be interpretable in terms of a renormalization-group operator, which should possess a strange attractor rather than a classical fixed point as in critical phenomena. In that sense, this self-similarity would contrast with the exact fixed-point recursive structure of snowflake fractals.

Since its implementation on a computer is not excessively time consuming and does not require enormous

storage,[101] the wavelet transform provides a very powerful tool for analyzing fractal aggregates of different kinds. The use of anisotropic analyzing wavelets enriched the capabilities of the wavelet microscope which may be applied to characterize directional phenomena or to detect the presence of local anisotropy in the aggregation process. Moreover, there is an alternative to the numerical wavelet transform of digitized pictures which consists in performing the wavelet transform using coherent optical spatial frequency filtering. An optical diffraction device has been recently designed in our laboratory and is currently performing what we have called the optical wavelet transform.[139] The ability of the optical wavelet transform to operate in real time provides a very efficient method for characterizing not only static but also dynamical phenomena. The application of the optical wavelet transform to a variety of experimental situations, e.g., percolation, colloidal aggregation, growth phenomena, propagation of fracture patterns, nucleation, two-dimensional melting, and turbulent flows, looks very promising.

ACKNOWLEDGMENTS

We would like to thank O. Thual for very interesting suggestions concerning the implementation of the 2D fast-Fourier transform in our wavelet transform algorithms. This work was supported by Centre National d'Etudes Spatiales, Grant No. APT-CNRS, CNES (Sciences Physiques en Microgravité). One of us (R.M.) is grateful to the unité FYMA (Université Catholique de Louvain, Louvain-la-Neuve) for its financial support and the Centre de Recherche Paul Pascal for its hospitality.

[1] *On Growth and Form: Fractal and Non-Fractal Patterns in Physics,* edited by H. E. Stanley and N. Ostrowsky (Nijhof, Dordrecht, 1986), and references quoted therein.

[2] *Fractals in Physics,* edited by L. Pietronero and E. Tosatti (North-Holland, Amsterdam, 1986), and references quoted therein.

[3] *Staphys 16,* edited by H. E. Stanley (North-Holland, Amsterdam, 1986), and references quoted therein.

[4] *The Physics of Structure Formation,* edited by W. Guttinger and D. Danglemayr (Springer-Verlag, Berlin, 1987), and references quoted therein.

[5] *Random Fluctuations and Pattern Growth,* edited by H. E. Stanley and N. Ostrowsky (Kluwer Academic, Dordrecht, 1988), and references quoted therein.

[6] T. A. Witten and L. M. Sander, Phys. Rev. Lett. **47**, 1400 (1981); Phys. Rev. B **27**, 5686 (1983).

[7] L. A. Turkevich and H. Scher, Phys. Rev. Lett. **55**, 1026 (1985).

[8] R. C. Ball, Physica **140A**, 62 (1986).

[9] T. C. Halsey, P. Meakin, and I. Procaccia, Phys. Rev. Lett. **56**, 854 (1986).

[10] M. Matsushita, K. Honda, H. Toyoki, Y. Hayakawa, and H. Kondo, J. Phys. Soc. Jpn. **55**, 2618 (1986).

[11] P. Meakin, Phys. Rev. A **27**, 1495 (1983).

[12] P. Meakin and Z. R. Wasserman, Chem. Phys. **91**, 391 (1984).

[13] P. Meakin and L. M. Sander, Phys. Rev. Lett. **54**, 2053 (1985).

[14] R. C. Ball and R. M. Brady, J. Phys. A **18**, L809 (1985).

[15] P. Meakin, Phys. Rev. A **33**, 3371 (1986).

[16] P. Meakin, R. C. Ball, P. Ramanlal, and L. M. Sander, Phys. Rev. A **35**, 5233 (1987).

[17] P. Meakin, in *Phase Transitions and Critical Phenomena,* edited by C. Domb and J. L. Lebowitz (Academic, Orlando, 1988) Vol. 12, and references quoted therein.

[18] T. Vicsek, Phys. Rev. Lett. **53**, 2281 (1984); Phys. Rev. A **32**, 3084 (1985).

[19] D. Bensimon, L. P. Kadanoff, S. Liang, B. I. Shraiman, and C. Tang, Rev. Mod. Phys. **58**, 977 (1986), and references quoted therein.

[20] J. R. Banavar, M. Kohmoto, and J. Roberts, Phys. Rev. A **33**, 2065 (1986).

[21] P. Meakin, F. Family, and T. Vicsek, J. Colloid Interface Sci. **117**, 394 (1987).

[22] R. Tao, M. A. Novotny, and K. Kaski, Phys. Rev. A **38**, 1019 (1988).

[23] J. Nittman and H. E. Stanley, J. Phys. A **20**, L1185 (1987).

[24] R. C. Ball, R. M. Brady, G. Rossi, and B. R. Thompson, Phys. Rev. Lett. **55**, 1406 (1985).

[25] M. Matsushita and H. Kondo, J. Phys. Soc. Jpn. **55**, 2483 (1986).

[26] J. Kertész and T. Viscek, J. Phys. A **19**, L257 (1986).

[27] P. Meakin, Phys. Rev. A **33**, 1984 (1986); **36**, 332 (1987).

[28] F. Family, D. E. Platt, and T. Viscek, J. Phys. A **20**, L1177 (1987).

[29] M. Kolb, Europhys. Lett. **4**, 85 (1987).

[30] P. Meakin and S. Havlin, Phys. Rev. A **36**, 4428 (1987).

[31] A. Renyi, *Probability Theory* (North-Holland, Amsterdam, 1970).

[32] P. Grassberger, Phys. Lett. **97A**, 227 (1983).

[33] H. G. E. Hentschel and I. Procaccia, Physica **8D**, 435 (1983).

[34] P. Grassberger and I. Procaccia, Physica **13D**, 34 (1984).

[35] E. B. Vul, Ya. G. Sinai, and K. M. Khanin, Usp. Mat. Nauk. **39**, 3 (1984) [J. Russ. Math. Surv. **39**, 1 (1984)].

[36] R. Benzi, G. Paladin, and A. J. Vulpiani, J. Phys. A **17**, 3521 (1984).

[37] G. Parisi (see appendix of U. Frisch), in *Turbulence and Predictability in Geophysical Fluid Dynamics and Climate Dynamics,* edited by M. Ghil, R. Benzi, and G. Parisi (North-Holland, Amsterdam, 1985), p. 84.

[38] T. C. Halsey, M. H. Jensen, L. P. Kadanoff, I. Procaccia, and B. I. Shraiman, Phys. Rev. A **33**, 1141 (1986).

[39] P. Collet, J. Lebowitz, and A. Porzio, J. Stat. Phys. **47**, 609 (1987).

[40] A. Arneodo, G. Grasseau, and M. Holschneider, in *Wavelets,* edited by J. M. Combes, A. Grossman, and P. Tchamitchian (Springer-Verlag, Berlin, 1989), p. 182.

[41] A. Arneodo, F. Argoul, J. Elezgaray, and G. Grasseau, in *Nonlinear Dynamics,* edited by G. Turchetti (World Scientific, Singapore, 1989), p. 130; A. Arneodo, F. Argoul, and G. Grasseau, Lect. Notes Math. (to be published).

[42] B. B. Mandelbrot, *The Fractal Geometry of Nature* (Freeman, San Francisco, 1982).

[43] A. Grossmann and J. Morlet, in *Mathematics and Physics, Lectures on Recent Results,* edited by L. Streit (World Scientific, Singapore, 1985).

[44] *Wavelets,* edited by J. M. Combes, A. Grossmann, and P.

Tchamitchian (Springer-Verlag, Berlin, 1989), and references quoted therein.
[45]P. Goupillaud, A. Grossmann, and J. Morlet, Geoexploration **23**, 85 (1984).
[46]A. Grossmann and J. Morlet, SIAM (Soc. Ind. Appl. Math.) J. Appl. Math. **15**, 723 (1984).
[47]A. Grossmann, J. Morlet, and T. Paul, J. Math. Phys. **26**, 2473 (1985); Ann. Inst. Henri Poincaré **45**, 293 (1986).
[48]P. G. Lemarie and Y. Meyer, Rev. Mat. Iberoam. **2**, 1 (1986).
[49]S. Jaffard and Y. Meyer, J. Math. Pures Appl. (to be published).
[50]I. Daubechies, Commun. Pure Appl. Math. **41**, 909 (1988).
[51]I. Daubechies and J. Lagarias, SIAM J. Math. Anal. (to be published).
[52]I. Daubechies, A. Grossmann, and Y. Meyer, J. Math. Phys. **27**, 1271 (1986).
[53]I. Daubechies and T. Paul, in *Proceedings of the VIIIth Congress of Mathematical Physics, Marseille, 1986,* edited by R. Seneor and M. Mebkhout (World Scientific, Singapore, 1987).
[54]T. Paul, Ph.D. thesis, University of Aix-Marseille II, France, 1985.
[55]A. Grossmann, M. Holschneider, R. Kronland-Martinet, and J. Morlet, Adv. Electron. Electron Phys. Suppl. **19** (to be published).
[56]G. Saracco, A. Grossmann, and P. Tchamitchian, in *Wavelets* (Ref. 44), p. 139.
[57]R. Kronland-Martinet, *Computer Music Journal* (MIT, Cambridge, MA, 1988), Vol. 12.
[58]S. G. Mallat, IEEE, Trans. PAMI (to be published); Trans. Am. Math. Soc. (to be published); and invited paper for a special issue on Multidmensional Signal Processing, IEEE Trans. Acoust. Speech Signal Process. (to be published).
[59]A. Grossmann, in *Stochastic Processes in Physics and Engineering,* edited by P. Blandard, L. Streit, and M. Hazewinkel (Reidel, Dordrecht, 1988).
[60]M. Hoschneider, J. Stat. Phys. **50**, 963 (1988) and Ph.D. thesis, University of Aix-Marseille II, France, 1988.
[61]A. Arneodo, G. Grasseau, and M. Holschneider, Phys. Rev. Lett. **61**, 2281 (1988).
[62]J. D. Farmer, E. Ott, and J. A. Yorke, Physica **7D**, 153 (1983).
[63]F. Argoul, A. Arneodo, G. Grasseau, Y. Gagne, E. J. Hopfinger, and U. Frisch, Nature **338**, 51 (1989).
[64]T. W. Burkhard and J. M. J. Van Leeuwen, *Real Space Renormalization* (Springer, Heidelberg, 1982).
[65]H. Gould, F. Family, and H. E. Stanley, Phys. Rev. Lett. **50**, 686 (1983).
[66]H. Nakanishi and F. Family, J. Phys. A **17**, 427 (1984).
[67]T. Nagatani, J. Phys. A **20**, L381 (1987); **20**, 6603 (1987); Phys. Rev. A **36**, 5812 (1987); **37**, 3514 (1988); **37**, 4461 (1988).
[68]L. Pietronero, A. Erzan, and C. Evertsz, Phys. Rev. Lett. **61**, 861 (1988).
[69]J. Nittman and H. E. Stanley, Nature **321**, 663 (1986).
[70]L. M. Sander P. Ramanlal, and E. Ben-Jacob, Phys. Rev. A **32**, 3160 (1985).
[71]L. M. Sander, in *Fractals in Physics* (Ref. 2), p. 241.
[72]P. Ramanlal and L. M. Sander, J. Phys. A **21**, L995 (1988).
[73]R. Murenzi, in *Wavelets* (Ref. 44), p. 239.
[74]F. Argoul, A. Arneodo, J. Elezgaray, G. Grasseau, and R. Murenzi, Phys. Lett. **135A**, 327 (1989).
[75]F. Argoul, A. Arneodo, J. Elezgaray, and G. Grasseau (unpublished).
[76]P. Meakin, Phys. Rev. A **34**, 710 (1986); **35**, 2234 (1987).
[77]C. Amitrano, A. Coniglio, and F. diLiberto, Phys. Rev. Lett. **57**, 1016 (1986).
[78]P. Meakin, A. Coniglio, H. E. Stanley, and T. A. Witten, Phys. Rev. A **34**, 3325 (1986).
[79]Y. Hayakawa, S. Sato, and M. Matsushita, Phys. Rev. A **36**, 1963 (1987).
[80]J. Lee and H. E. Stanley, Phys. Rev. Lett. **61**, 2945 (1988).
[81]R. Ball and M. Blunt, Phys. Rev. A **39**, 3591 (1989).
[82]S. Ohta and H. Honjo, Phys. Rev. Lett. **60**, 611 (1988).
[83]M. Blunt and P. King, Phys. Rev. A **37**, 3935 (1988).
[84]L. M. Sander, in *The Physics of Structure Formation* (Ref. 4), p. 257.
[85]D. G. Grier, D. A. Kessler, and L. M. Sander, Phys. Rev. Lett. **59**, 2315 (1987).
[86]D. G. Grier, E. Ben-Jacob, R. Clarke, and L. M. Sander, Phys. Rev. Lett. **56**, 1264 (1986).
[87]Y. Sawada, A. Dougherty, and J. P. Gollub, Phys. Rev. Lett. **56**, 1260 (1986).
[88]R. M. Brady and R. C. Ball, Nature **309**, 225 (1984).
[89]M. Matsushita, M. Sano, Y. Hayakawa, H. Honjo, and Y. Sawada, Phys. Rev. Lett. **53**, 286 (1984).
[90]M. Matsushita, Y. Hayakawa, and Y. Sawada, Phys. Rev. A **32**, 3814 (1985).
[91]F. Argoul, A. Arneodo, G. Grasseau, and H. L. Swinney, Phys. Rev. Lett. **61**, 2558 (1988).
[92]J. P. Eckmann and D. Ruelle, Rev. Mod. Phys. **57**, 617 (1985).
[93]See, for example: T. Bohr and T. Tél, in *Directions in Chaos,* edited by Hao Bai-Lin (World Scientific, Singapore, 1988) Vol. 2; T. Tél Z. Naturforsch **43A**, 1154 (1988); R. Badii, Ph.D. thesis, Zurich (1987); M. J. Feigenbaum, J. Stat. Phys. **46**, 919 and 925 (1987).
[94]B. Mandelbrot, J. Fluid Mech. **62**, 331 (1974).
[95]R. Badii and A. Politi, Phys. Lett. **104A**, 303 (1984).
[96]L. A. Smith, J. D. Fourier, and E. A. Speigel, Phys. Lett. **114A**, 465 (1986).
[97]D. Bessis, J. D. Fournier, G. Servizi, G. Turchetti, and S. Vaienti, Phys. Rev. A **36**, 920 (1987).
[98]A. Arneodo, G. Grasseau, and E. J. Kostelich, Phys. Lett. **124A**, 426 (1987).
[99]F. Argoul, A. Arneodo, and G. Grasseau, Z. Angew. Math. Mech. **68**, 519 (1988).
[100]P. Grassberger, R. Badii, and A. Politi, J. Stat. Phys. **51**, 135 (1988).
[101]G. Grasseau, Ph.D. thesis, University of Bordeaux I, France, 1989.
[102]H. Froehling, J. P. Crutchfield, D. Farmer, N. H. Packard, and R. Shaw, Physica **3D**, 605 (1981).
[103]P. Grassberger and I. Procaccia, Phys. Rev. Lett. **50**, 346 (1983); Physica **9D**, 189 (1983).
[104]R. Badii and A. Politi, Phys. Rev. Lett. **52**, 1661 (1984); J. Stat. Phys. **40**, 725 (1985).
[105]R. Badii and G. Broggi, Phys. Lett. **131A**, 131 (1988).
[106]B. B. Mandelbrot, in *Random Fluctuations and Pattern Growth* (Ref. 5), p. 279.
[107]W. Van der Water and P. Schram, Phys. Rev. A **37**, 3118 (1988).
[108]A. Chhabra and R. V. Jensen, Phys. Rev. Lett. **62**, 1327 (1989); A. B. Chhabra, C. Meneveau, R. V. Jensen, and K. R. Sreenivasan, Phys. Rev. A **40**, 5284 (1989).
[109]P. Hanusse, in *Wavelets* (Ref. 44), p. 305.
[110]R. Murenzi, Ph.D. thesis, Université Catholique de Louvain-la-Neuve (1990).
[111]J. M. Ghez and S. Vaienti, J. Stat. Phys. **57**, 415 (1989).
[112]J. S. Langer, Rev. Mod. Phys. **52**, 1 (1980); in *Staphys 16* (Ref. 3), p. 44; in *Chance and Matter,* edited by J. Souletie, J.

Vanimenus, and R. Stora (North-Holland, Amsterdam, 1987).
[113]U. Nakaya, *Snow Crystals* (Harvard University Press, Harvard, 1954).
[114]W. A. Bentley and W. T. Humphreys, *Snow Crystals* (Dover, New York, 1962).
[115]T. Vicsek, J. Phys. A **16**, L647 (1983).
[116]As far as the transition to chaos is concerned, the support of the invariant measure corresponding to the critical golden-mean trajectory is not lacunar (it is the whole circle), but its wavelet transform displays oscillating power-law behavior as shown in Refs. 40, 41, and 61.
[117]M. Kolb, J. Phys. Lett. **46**, L631 (1985).
[118]P. Meakin and F. Family, Phys. Rev. A **34**, 2558 (1986).
[119]P. Meakin, Phys. Rev. A **33**, 4199 (1986).
[120]J. Nittmann, G. Daccord, and H. E. Stanley, Nature **314**, 141 (1985).
[121]P. Meakin, J. Phys. A **18**, L661 (1985).
[122]L. Paterson, J. Fluid Mech. **133**, 513 (1981).
[123]S. N. Rauseo, P. D. Barnes, and J. V. Maher, Phys. Rev. A **35**, 1245 (1987).
[124]A. R. Kopf-Sill and G. M. Homsy, Phys. Fluids **31**, 242 (1988).
[125]Y. Couder, in *Random Fluctuations and Pattern Growth* (Ref. 5), p. 75.
[126]H. Thomé, M. Rabaud, V. Hakim, and Y. Couder, Phys. Fluids A **1**, 224 (1989).
[127]G. Daccord, J. Nittmann, and H. E. Stanley, Phys. Rev. Lett. **56**, 336 (1986).
[128]I. Procaccia and R. Zeitak, Phys. Rev. Lett. **60**, 2511 (1988).
[129]G. M. Dimino and J. H. Kaufman, Phys. Rev. Lett. **62**, 2277 (1989).
[130]F. Argoul, A. Arneodo, Y. Couder, V. Hakim, and M. Rabaud, (unpublished).
[131]A. Arneodo, Y. Couder, G. Grasseau, V. Hakim, and M. Rabaud, Phys. Rev. Lett. **63**, 984 (1989).
[132]P. Meakin and T. Vicsek, Phys. Rev. A **32**, 685 (1985).
[133]T. C. Halsey and P. Meakin, Phys. Rev. A **32**, 2546 (1985).
[134]*Universality in Chaos,* edited by P. Cvitanovic (Hilger, Bristol, 1984), and references quoted therein.
[135]*Chaos,* edited by Bai-Lin Hao (World Scientific, Singapore, 1984), and references quoted therein.
[136]H. G. Schuster, *Deterministic Chaos* (Physik-Verlag, Weinheim, 1984), and references quoted therein.
[137]P. Berge, Y. Pomeau, and C. Vidal, *Order within Chaos* (Wiley, New York, 1986), and references quoted therein.
[138]F. Argoul, A. Arneodo, J. Elezgaray, and G. Grasseau, in *Proceedings of the International Workshop on Quantitative Measures of Dynamical Complexity in Nonlinear Systems, Bryn Mawr College, 1989* (Plenum, New York, in press).
[139]E. Freysz, B. Pouligny, F. Argoul, and A. Arneodo, Phys. Rev. Lett. **64**, 745 (1990).

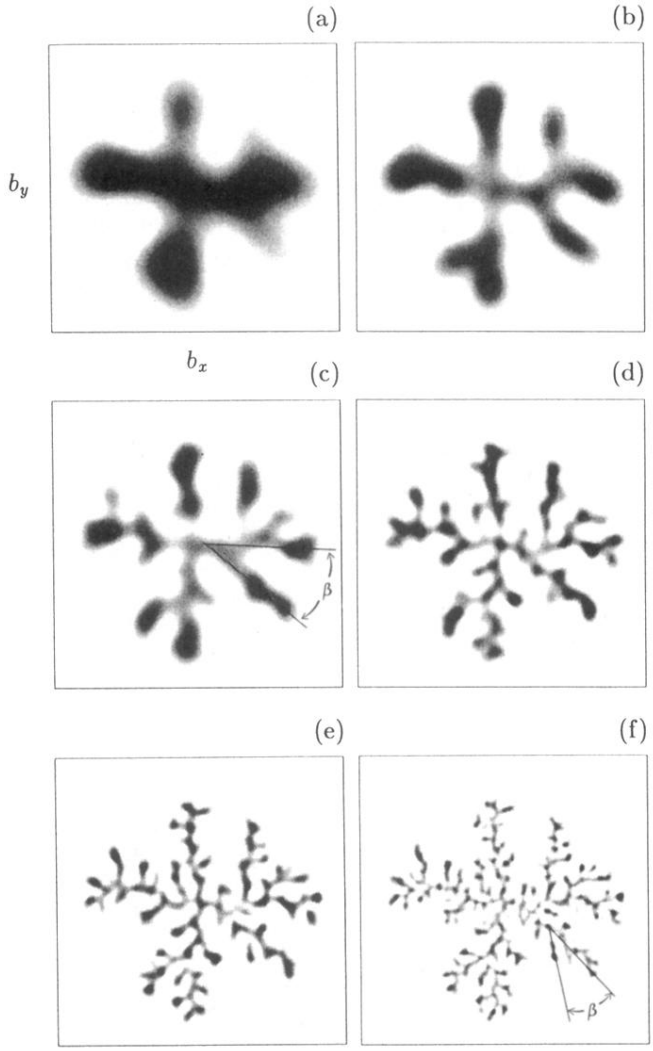

FIG. 14. Wavelet transforms of the ($M=5465$ particles) DLA cluster shown in Fig. 13(a). $T_g(a,\mathbf{b})$ is coded using 32 shades from white ($T_g \leq 0$) to black ($\max T_g > 0$) for each value of the scale parameter (a) $a = a^*$, (b) a^*/δ, (c) a^*/δ^2, (d) a^*/δ^3, (e) a^*/δ^4, and (f) a^*/δ^5 where $\delta = 1.55$. An average angle $\langle \beta \rangle$ can be defined over a wide range of scales as characterizing screening effects in DLA growth process. The analyzing wavelet is defined in Eq. (3.23).

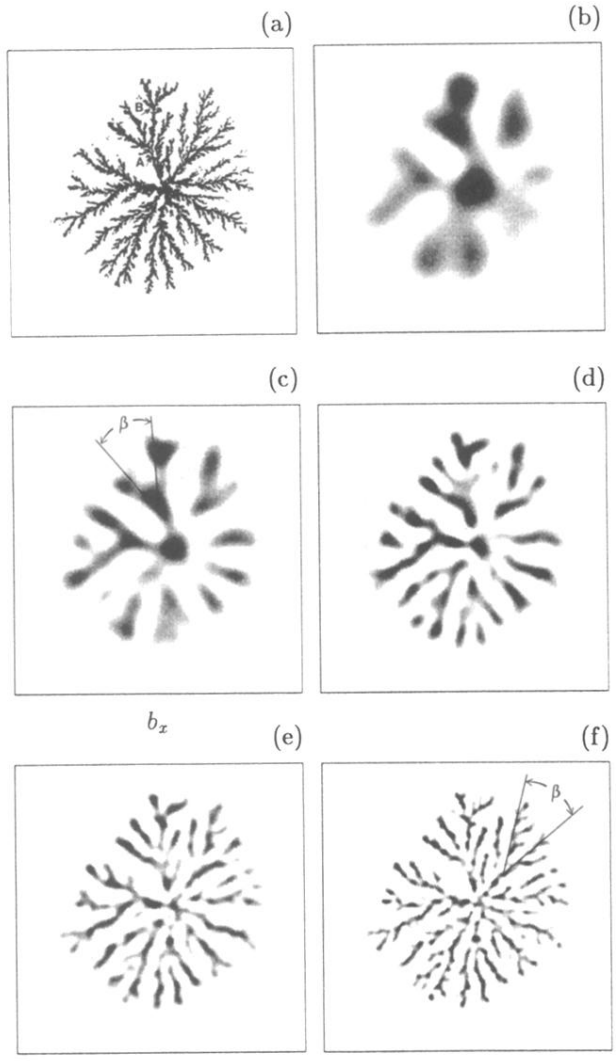

FIG. 19. Wavelet transforms of the copper electrodeposition cluster shown in (a). $T_g(a,\mathbf{b})$ is coded using 32 shades from white ($T_g \leq 0$) to black ($\max T_g > 0$) for each value of the scale parameter (b) $a = a^*$, (c) a^*/δ, (d) a^*/δ^2, (e) a^*/δ^3, and (f) a^*/δ^4 where $\delta = 1.55$. An average angle $\langle\beta\rangle \sim 36°$ can be defined over a wide range of scales as characterizing screening effects in electrodeposition process. The analyzing wavelet is defined in Eq. (3.23).

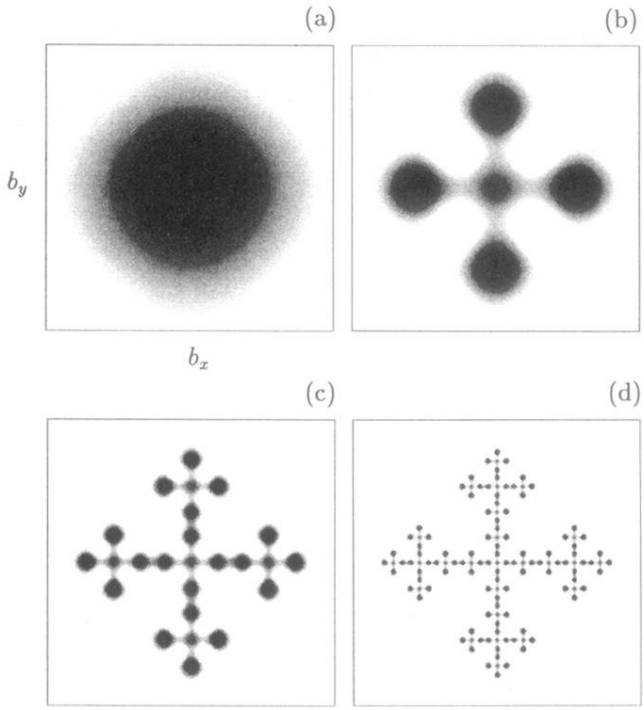

FIG. 5. Wavelet transforms of the one-scale snowflake fractal shown in Fig. 4(a). $T_g(a,\mathbf{b})$ is coded using 32 shades from white ($T_g \leq 0$) to black ($\max T_g > 0$) for each value of the scale parameter (a) $a = a^*$, (b) $a^*/3$, (c) $a^*/3^2$ and, (d) $a^*/3^3$. The analyzing wavelet is defined in Eq. (3.23).

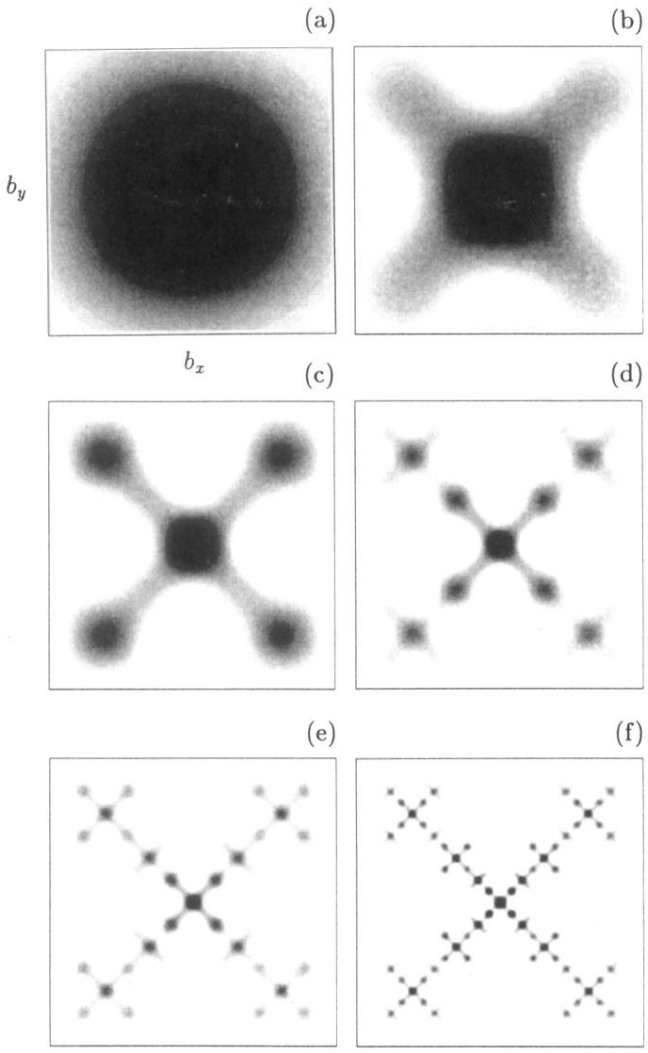

FIG. 9. Wavelet transforms of the two-scale snowflake fractal shown in Fig. 8(a). $T_g(a,\mathbf{b})$ is coded using 32 shades from white ($T_g \leq 0$) to black ($\max T_g > 0$) for each value of the scale parameter (a) $a = a^*$, (b) $a^*/2$ (c) $a^*/2^2$, (d) $a^*/2^3$, (e) $a^*/2^4$, and (f) $a^*/2^5$. The analyzing wavelet is defined in Eq. (3.23).